

# *Bayesian retrieval of complete posterior PDFs of oceanic rain rate from microwave observations*

Article

Published Version

Chiu, J. C. and Petty, G.W. (2006) Bayesian retrieval of complete posterior PDFs of oceanic rain rate from microwave observations. *Journal of Applied Meteorology and Climatology*, 45 (8). pp. 1073-1095. ISSN 1558-8424 doi: 10.1175/JAM2392.1 Available at <https://centaur.reading.ac.uk/16771/>

It is advisable to refer to the publisher's version if you intend to cite from the work. See [Guidance on citing](#).

To link to this article DOI: <http://dx.doi.org/10.1175/JAM2392.1>

Publisher: American Meteorological Society

All outputs in CentAUR are protected by Intellectual Property Rights law, including copyright law. Copyright and IPR is retained by the creators or other copyright holders. Terms and conditions for use of this material are defined in the [End User Agreement](#).

[www.reading.ac.uk/centaur](http://www.reading.ac.uk/centaur)

**CentAUR**

Central Archive at the University of Reading

Reading's research outputs online

## Bayesian Retrieval of Complete Posterior PDFs of Oceanic Rain Rate from Microwave Observations

J. CHRISTINE CHIU

*Joint Center for Earth Systems Technology, University of Maryland, Baltimore County, Baltimore, Maryland*

GRANT W. PETTY

*Department of Atmospheric and Oceanic Sciences, University of Wisconsin—Madison, Madison, Wisconsin*

(Manuscript received 5 May 2005, in final form 12 December 2005)

### ABSTRACT

A new Bayesian algorithm for retrieving surface rain rate from Tropical Rainfall Measuring Mission (TRMM) Microwave Imager (TMI) over the ocean is presented, along with validations against estimates from the TRMM Precipitation Radar (PR). The Bayesian approach offers a rigorous basis for optimally combining multichannel observations with prior knowledge. While other rain-rate algorithms have been published that are based at least partly on Bayesian reasoning, this is believed to be the first self-contained algorithm that fully exploits Bayes's theorem to yield not just a single rain rate, but rather a continuous posterior probability distribution of rain rate. To advance the understanding of theoretical benefits of the Bayesian approach, sensitivity analyses have been conducted based on two synthetic datasets for which the "true" conditional and prior distribution are known. Results demonstrate that even when the prior and conditional likelihoods are specified perfectly, biased retrievals may occur at high rain rates. This bias is not the result of a defect of the Bayesian formalism, but rather represents the expected outcome when the physical constraint imposed by the radiometric observations is weak owing to saturation effects. It is also suggested that both the choice of the estimators and the prior information are crucial to the retrieval. In addition, the performance of the Bayesian algorithm herein is found to be comparable to that of other benchmark algorithms in real-world applications, while having the additional advantage of providing a complete continuous posterior probability distribution of surface rain rate.

### 1. Introduction

Satellite passive microwave observations are now widely used to estimate global surface rainfall (Adler et al. 2001). Inference of surface rainfall  $R$  from microwave brightness temperatures  $T_B$  would be less troublesome if the relationship between these two variables were unique and reasonably linear. Unfortunately, not only is the relationship nonmonotonic, owing to the competing effects of scattering and emission (Petty 1994a), but a variety of microphysical and environmental factors introduces significant variability into the relationship. This ambiguity is compounded by spatial variability in the rain intensity when the strongly non-

linear function of local rain rate is averaged over a finite instrument field of view (FOV) of the order of 10 km or larger (Wilheit 1986; Petty 1994a,b). As a result, the rainfall retrieval problem requires not only a suitable physical model, but also a proper accounting for the statistical variability in the relationship between FOV-averaged rain rate and FOV-averaged microwave observables.

Bayes's theorem states that for a given observation vector  $\mathbf{P}$  (e.g., multichannel microwave observations), the posterior probability distribution of the parameter  $R$  to be estimated (e.g., rain rate) is proportional to the conditional likelihood times the prior distribution,

$$\pi(R|\mathbf{P}) \propto f(\mathbf{P}|R) \cdot \pi(R), \quad (1)$$

where  $f(\mathbf{P}|R)$  is a conditional probability density function (PDF) that specifies the probability distribution of the observation  $\mathbf{P}$  given parameter  $R$ . Because this dis-

---

Corresponding author address: J. Christine Chiu, NASA/GSFC, Code 613.2, Greenbelt, MD 20771.  
E-mail: cchiu@climate.gsfc.nasa.gov

tribution incorporates information concerning the physical response of the observations  $\mathbf{P}$  to the parameter  $R$  (as well as the statistical variability in that response), we will refer to this part as the physical model. Our prior knowledge of the parameter is summarized by  $\pi(R)$  before data are seen. The interaction of the physical model and the prior (e.g., climatological) probability distribution of  $R$  determines the so-called *posterior distribution*  $\pi(R|\mathbf{P})$ , that is, the new PDF of  $R$  in light of the observations  $\mathbf{P}$ . Normally, the effect of  $\mathbf{P}$  is to reduce the spread of  $\pi(R|\mathbf{P})$  relative to  $\pi(R)$ ; the degree of reduction is a measure of the information content of  $\mathbf{P}$ .

Bayes's theorem is not an algorithm per se, but it offers a rigorous and completely general theoretical framework for retrieving atmospheric variables from remote sensing measurements. The major practical obstacle to its routine application is the need to specify the prior distribution  $\pi(R)$  and conditional distribution  $f(\mathbf{P}|R)$ . When the parameter  $R$  is a scalar, the specification of the first of these poses no major difficulty. It is more difficult when the parameter to be retrieved is an  $N$ -dimensional vector (e.g., a hydrometeor profile), because the prior distribution is then a multivariate function that must typically be estimated from a very large ensemble of model simulations. For example, a number of papers have explicitly invoked Bayes's theorem in the design of an algorithm to infer rain rate and other rain cloud properties from multichannel microwave radiances (Evans et al. 1995; Kummerow et al. 1996, 2001; Olson et al. 1996, 2006; Bauer et al. 2001; Marzano et al. 2002; Tassa et al. 2003; Di Michele et al. 2005). These typically attempt to retrieve a single so-called best vertical hydrometeor profile and an associated surface rain rate.

Regardless of whether  $R$  is a scalar or a vector, the accurate specification of  $f(\mathbf{P}|R)$  can pose a major challenge, because it depends on accurate modeling of both the physical and statistical properties of the mapping from  $R$  to the observation vector  $\mathbf{P}$ . The higher the dimensionality of both, the more difficult it is to obtain a sufficiently large and varied sample of either observations or simulations to accurately represent conditional distribution.

Partly for this reason, we are unaware of any previous algorithm that fully exploits Bayes's theorem to explicitly provide a continuous posterior PDF of rain rate. Rather, the above algorithms are generally formulated so as to yield a single surface rain rate for each sensor FOV. In the Goddard profiling algorithm (GPROF) (Kummerow et al. 1996; Olson et al. 1996), the Bayes method is essentially reduced to a table lookup. Consequently, retrievals from GPROF are de-

termined only by how close the observation vector is to the nearest candidates of the database, and by how often similar cloud profiles occur in the database. Furthermore, existing Bayesian retrieval algorithms depend on the representativeness of independent cloud radiative databases and on assumptions about the form of conditional and prior likelihoods (e.g., Gaussian properties), even though training data are known to disagree with those assumptions to at least some degree.

Here we describe a new Bayesian algorithm for rain-rate retrieval over the ocean using dual-polarization passive microwave images from the conically scanning Tropical Rainfall Measuring Mission (TRMM) Microwave Imager (TMI). Unlike previous algorithms, this one is based on explicit numerical evaluation of (1). We are able to do this in part because we limit our attention to a low-dimensional problem—estimating a single scalar FOV-averaged rain rate  $R$  from only three microwave observables [the attenuation index  $\mathbf{P}$  (defined below) at 10.65, 19.35, and 37 GHz].

This new algorithm has two unique characteristics. Unlike other Bayesian methods, ours is based on explicit mathematical models of the conditional likelihood  $f(\mathbf{P}|R)$  and the prior distribution  $\pi(R)$ , based on empirical fits to data derived from both simulations and actual observations. Most importantly, unlike other methods, the result of our method is not a single best rain rate, but rather a complete posterior probability distribution. A major shortcoming of existing rain-rate retrieval methods has been the lack of a basis for systematically and rigorously characterizing uncertainty. Particularly in view of the highly skewed distribution of rain rates and the nonlinear response of microwave radiometers to surface rainfall, the quantification of uncertainty is complicated by the likelihood that errors will be non-Gaussian. The lack of quantitative error information in turn hampers the optimal assimilation of rain-rate estimates into models. Efforts have been made in quantifying the inherent uncertainty of retrieved rain rates in GPROF (Olson et al. 2006) and the Bayesian Algorithm for Microwave-Based Precipitation Retrieval (BAMPR) (Tassa et al. 2003; Di Michele et al. 2005) from selected cloud profiles of databases. However, the algorithm described in this paper shows that it is possible to directly apply Bayes's theorem so that, given an observation vector from the TMI, one may obtain a complete posterior PDF of rain rate rather than merely a single best estimate of rain rate at that location.

This paper focuses on (a) the algorithm definition, (b) key aspects of the performance of the Bayesian methodology under controlled conditions, and (c) applications to TMI data. There are several components

to (b). The first pertains to the performance of a Bayesian rain-rate algorithm under ideal conditions, that is, when both  $f(\mathbf{P}|R)$  and  $\pi(R)$  are specified perfectly. We will show that, even under such ideal conditions, systematic biases in retrieved intensity are a natural result when the physical information in the observations is insufficient to strongly constrain the results (e.g., in high rain rates, where saturation of microwave radiances tends to occur).

Because the “true”  $f(\mathbf{P}|R)$  and  $\pi(R)$  are normally only approximately known for real-world retrievals, the second component of our sensitivity analysis pertains to the influence of errors in the specification of these functions on the quality of the retrievals. Evans et al. (1995), using simulated data, evaluated which covariates had the greatest influence on the accuracy of retrievals. Nevertheless, their results were subject also to imperfections in the cloud model and radiative transfer model, as well as to simplifying assumptions built into both their conditional and prior distributions. Unlike their work, we describe the results of sensitivity tests using two synthetic datasets where the true conditional and prior distributions are perfectly known. We are therefore able to examine the intrinsic limits in the retrievability of rain rate (based on our observables) without regard to possible errors in the models themselves.

There is the important question of how to interpret the resulting posterior rain-rate PDF in terms of a single best rain rate for any given sensor FOV. We will show that, owing to the highly skewed properties of the posterior PDF, the choice of estimator (e.g., maximum likelihood versus minimum variance or expectation value) is of critical importance and needs to be selected carefully with the particular application in mind. Note that the former was used in Evans et al. (1995) and referred to as the maximum a posteriori probability (MAP) in Marzano et al. (1999), while the latter was used in GPROF and BAMPR and referred to as minimum mean square (MMS) criterion in Tassa et al. (2003) and Di Michele et al. (2005).

Applications to TMI data include implements of our new Bayesian rain-rate retrieval algorithm and validations against estimates from TRMM precipitation radar (PR). The PR is an active microwave sensor that scans in a cross-track strategy from nadir to  $17^\circ$ . The swath width is about 215 km and the minimum detectable threshold of PR reflectivity is about 17 dBZ in the absence of attenuation. The horizontal resolution is about 4.3 km at nadir, while the vertical resolution is 0.25 km. In addition, we compare performance of our Bayesian algorithm with that of other benchmark algorithms. The algorithm may be judged successful if its

overall performance at estimating surface rain rate (based on an appropriate estimator applied to the posterior PDF, such as the expectation value) is not significantly worse than that of other algorithms, while also providing the detailed error information that other algorithms lack.

In the next section, we begin by reviewing the definition of the normalized polarization (or attenuation index)  $\mathbf{P}$  (Petty 1994a). Because of certain desirable properties, this linear transformation of dual-polarization brightness temperatures serves as the fundamental microwave “observable” in our algorithm. In section 3, we introduce highly simplified but reasonably realistic analytic models for the local dependence of  $\mathbf{P}$  on local rain rate at each frequency. The statistical variability of this relationship resulting from spatial averaging over realistically nonuniform rainfall is then evaluated by applying these relationships to a large set of radar-derived rain-rate fields. We show that the statistical distribution of our simulated  $\mathbf{P}$  in 3D space is similar to that observed in actual observations of oceanic rainfall by the TMI. Section 4 describes the construction of the prior and conditional distribution functions required by the Bayesian algorithm. The design and results of the sensitivity tests are discussed in section 5. Section 6 presents real-world applications and validation of this Bayesian algorithm, followed by summary and discussions.

## 2. TMI attenuation indices $\mathbf{P}$

### a. Instrument description

The TMI measures dual-polarized brightness temperatures at 10.65, 19.35, 37.00, and 85.50 GHz, and vertical polarization-only brightness temperatures at 21.3 GHz. Detailed descriptions of other TMI characteristics can be found in Kummerow et al. (1998) and Bauer and Bennartz (1998). For convenience, we henceforth denote vertically polarized brightness temperatures at TMI channels as  $T_{10V}$ ,  $T_{19V}$ ,  $T_{21V}$ ,  $T_{37V}$ , and  $T_{85V}$ , and replace V with H for horizontal polarization.

As discussed by Petty (1994a), individual channel brightness temperatures have significant shortcomings as the primary observables in a physically based rain-rate retrieval algorithm. Each channel, regardless of whether it is horizontally or vertically polarized, will respond to a variety of environmental variables, as well as to a mixture of both emission and scattering from the rain cloud itself. Petty therefore proposed the use of linear transformations of dual-polarization brightness temperatures  $T_V$  and  $T_H$  at any given frequency. These effectively decouple the emission (attenuation) and

scattering contributions into two separate variables,  $P$  and  $S$ , as well as factor out background variability resulting from variations in atmospheric water vapor, surface roughness, and so on.

### b. Definition

We limit our attention here to the attenuation index (or normalized polarization)  $P$ , which is defined as

$$P \equiv \frac{T_V - T_H}{T_{V,O} - T_{H,O}}, \quad (2)$$

where  $T_V$  and  $T_H$  are the vertically and horizontally polarized brightness temperatures;  $T_{V,O}$  and  $T_{H,O}$  are the estimated or modeled brightness temperatures in the absence of rain or cloud. Ideally, the value of  $P$  therefore falls in the range  $[0, 1]$ , where 1 corresponds to a cloud-free pixel, and values approaching 0 represent a very opaque atmospheric condition generally associated with heavy precipitation.

The use of the attenuation index  $P$  in the retrieval algorithm has three advantages. First, unlike brightness temperature, it decreases monotonically with increasing rainfall intensity. Second, the attenuation index is not sensitive to the background variability because  $P$  is mainly determined by rain cloud optical thickness. Third, for the special case of a horizontally homogeneous rain layer,  $P$  and transmittance  $t$  obey an approximate power-law relationship,  $P \equiv t^\alpha$ , with  $\alpha \approx 1.7$ . Therefore, in this limiting case, the  $P$  index yields a direct indication of the rain cloud transmittance. In this paper, our microwave observables are the attenuation indices at 10.65, 19.35, and 37.0 GHz. Our observation vector  $\mathbf{P}$  is therefore given by  $(P_{10}, P_{19}, P_{37})$ .

### c. Implementation for TMI

To convert satellite-observed brightness temperatures  $T_V$  and  $T_H$  at a given frequency to the attenuation index  $P$ , we require estimates of the cloud-free background brightness temperatures  $T_{V,O}$  and  $T_{H,O}$ . To a good approximation, these are functions of total column water vapor  $V$  and surface wind speed  $U$ . Both of these variables may be directly estimated from the passive microwave observations themselves, provided that care is taken to exclude FOVs contaminated by rain or land. The retrieved fields of  $V$  and  $U$  are then spatially interpolated into areas of precipitation and used as the basis for estimating  $T_{V,O}$  and  $T_{H,O}$ . It is not essential that these estimates be very precise, only that they account for most of the variation in the background polarization difference  $T_{V,O} - T_{H,O}$ . Uncertainties in the estimate of this quantity are treated as part of the inherent observational error in  $P$ .

We derived our own empirical algorithms for  $V$  and  $U$  from matchups between TMI radiances and surface observations. For column water vapor, we matched radiosonde observations to TMI overpasses in January and July 1999. The matchup procedure was similar to Alishouse et al. (1990) and Petty (1994b). Further details are given in Chiu (2003). The resulting statistical water vapor algorithm ( $\text{kg m}^{-2}$ ) is given by

$$\begin{aligned} V = & 128.57 + 33.94 \ln(290 - T_{19V}) \\ & - 72.13 \ln(290 - T_{21V}) \\ & + 10.48 \ln(290 - T_{37H}). \end{aligned} \quad (3)$$

Matchups between the TMI measurements and surface buoy wind data from the National Oceanic and Atmospheric Administration (NOAA) Marine Environmental Buoy database (Chiu 2003) yielded the following algorithm for wind speed ( $\text{m s}^{-1}$ ):

$$\begin{aligned} U = & 130.908 + 0.170T_{10V} + 0.128T_{10H} \\ & - 0.034T_{19V} - 0.115T_{19H} - 0.079T_{21V} \\ & - 1.121T_{37V} + 0.543T_{37H}. \end{aligned} \quad (4)$$

Empirical expressions for the background brightness temperatures were derived from 489 TMI orbits in July 1999:

$$\begin{aligned} T_{10V,O} &= 154.1 + 0.076V + 0.24U + 0.47T_S, \\ T_{10H,O} &= 73.8 + 0.14V + 0.90U + 0.24T_S, \\ \ln(300 - T_{19V,O}) &= 4.89 - 0.0072V - 0.0017U \\ &\quad - 0.0025T_S, \\ \ln(300 - T_{19H,O}) &= 5.39 - 0.0078V - 0.0063U \\ &\quad - 0.00052T_S, \\ \ln(300 - T_{37V,O}) &= 4.65 - 0.0058V + 0.00055U \\ &\quad - 0.00069T_S, \text{ and} \\ \ln(300 - T_{37H,O}) &= 5.22 - 0.0065V - 0.0080U \\ &\quad + 0.00031T_S, \end{aligned} \quad (5)$$

where  $V$  and  $U$  were estimated by (3) and (4), and sea surface temperature  $T_S$  ( $^{\circ}\text{C}$ ) was obtained from a climatological database [obtained from the National Aeronautics and Space Administration (NASA) Goddard Space Flight Center (GSFC)].

## 3. Radar-radiative simulations

### Simulated $P$ for realistic rain fields

A key part of our algorithm is the specification of  $f(\mathbf{P}|R)$ , which depends on both the physical and statis-



tical properties of rainfall, especially the variable effects of beam filling, which we take to be the single most important factor determining the normalized polarization (this is not true for the single-channel brightness temperatures). Because actual matchup data from microwave and rainfall measurements or detailed model simulations do not exist in a sufficient quantity, we rely on simulated data derived from high-resolution radar composites.

### 1) RADAR DATA

As previously mentioned, beam-filling errors owing to inhomogeneities of rain clouds result in a nonunique relationship between rain rate and microwave signal, and these contribute to significant ambiguities in passive microwave retrievals. To account for rain cloud inhomogeneity in our specification of  $f(\mathbf{P}|R)$ , we used the National Weather Service (NWS) Weather Surveillance Radar-1988 Doppler (WSR-88D) radar operational reflectivity data to obtain spatially realistically rain-rate fields for use in simple radiative transfer simulations designed to capture the contribution of horizontal inhomogeneity to fluctuations in the  $P$ – $R$  relationship for any given frequency.

The reflectivity data were operational gridded composites of 154 NWS WSR-88D sites in the United States with an hourly temporal resolution and a spatial resolution of 1 km. Reflectivity values were converted to rain rate using the Marshall and Palmer (1948) relationship  $Z = 200R^{1.6}$ . (This relationship is intended only to yield statistically reasonable spatial patterns of rain intensity for use in the simulations, not absolutely calibrated rain-rate estimates.) A total of 22 radar reflectivity files were randomly selected during July and August 2002, each comprising an average of  $3 \times 10^4$  rainy pixels. Because of the coarseness of the digitization of reflectivity  $Z$ , small upward and downward shifts in  $Z$  were applied to each image in order to yield a reasonably smooth combined histogram of modeled rain rates. This procedure effectively multiplied the number of radar grids to 110. The reader is referred to Chiu (2003) for additional details.

### 2) POLARIZATION CALCULATIONS

Starting with the precipitation structures simulated from the radar measurements, we simulated satellite-observed polarization  $P$  via a simplified plane-parallel radiative transfer model. The mass extinction coefficient of suspended cloud water  $\kappa_{e,l}$  is listed in Table 1, which was computed from Liebe et al. (1991) assuming a temperature of 0°C. The relationship between the volume extinction coefficients of rain  $k_{e,r}$  and rain rates

TABLE 1. Parameters  $a$  and  $b$  in the approximation of liquid water extinction coefficient.

Channel (GHz)	$\kappa_{e,l}$ ( $\text{m}^2 \text{ kg}^{-1}$ )	$a$	$b$
10.65	0.0244	0.002 956	1.187 59
19.35	0.0785	0.015 85	1.094 03
37.00	0.261	0.068 96	1.018 76
85.50	0.932	0.2799	0.846 93

( $R$ ) was estimated from Mie theory, assuming spherical raindrops with a liquid water temperature of 10°C and Marshall–Palmer drop size distribution. A power-law form was found to approximate the relationship well (Petty 1994b),

$$k_{e,r} = aR^b, \quad (6)$$

where coefficients  $a$  and  $b$  for each channel are shown in Table 1. The rain-layer optical depth  $\tau_r$  was then modeled as

$$\tau_r \cong Z_f k_{e,r}(R), \quad (7)$$

representing the contribution of suspended rain to attenuation of the polarized ocean surface emission. Because there was no information about the values of the freezing height  $Z_f$  in the radar reflectivity product, a fixed value of 3 km was assumed for the purposes of this demonstration. The optical depth  $\tau_l$  attributed to suspended cloud water was modeled as

$$\tau_l = \kappa_{e,l}L, \quad (8)$$

where variations in the suspended cloud water content  $L$  ( $\text{kg m}^{-2}$ ) were simulated via a lognormal random deviate applied to each grid cell.

Because depolarization of the ocean surface emission by rain clouds depends primarily on total path attenuation and not on the details of the vertical structure of temperature or hydrometeor properties, we may use a highly simplified 1D plane-parallel model to compute brightness temperatures at each grid point. The radiative transfer equation is written as

$$T_{B,p} = (1 - t)T_A + \varepsilon_p t T_S + (1 - t)(1 - \varepsilon_p)t T_A, \quad (9)$$

where the simulated brightness temperature  $T_{B,p}$  at polarization  $p$  (vertical or horizontal) is determined by the transmittance  $t$ , the specular emissivity of the surface (ocean in the study)  $\varepsilon_p$ , the surface temperature  $T_S$ , and the air temperature  $T_A$ . The transmittance  $t$  is given by

$$t = \exp\left(-\frac{\tau}{\cos\theta}\right), \quad (10)$$

where  $\theta$  is the incidence angle and  $\tau$  is the total optical depth due to hydrometeors. The surface temperature was approximated from the extrapolation of the temperature profile, assuming a temperature at the freezing level of  $0^\circ\text{C}$  and a lapse rate of  $6.5\text{ K km}^{-1}$ . Here  $T_A$  was estimated by the air temperature at the midpoint between the surface and  $Z_f$ . Because the emissivity of the ocean is polarized, both the vertically and horizontally polarized radiance was obtained.

We define  $t_a$ ,  $t_b$ , and  $t_r$  as the transmittance attributed to the atmosphere, the suspended cloud water, and the rain, respectively, and  $t_1$  as the total transmittance (the product  $t_a$ ,  $t_b$ , and  $t_r$ ). Based on (2) and (9), it can be shown that the attenuation index (normalized polarization) can be written as

$$P = \frac{t_1(T_S - T_A) + t_1^2 T_A}{t_a(T_S - T_{A,O}) + t_a^2 T_{A,O}}, \quad (11)$$

where  $T_{A,O}$  represents the air temperature when the suspended cloud water and rain are absent. We assume  $T_A \approx T_{A,O}$  in the simulations. In addition, the order of the first term for both the numerator and denominator is much smaller than the second term. Therefore, the attenuation index can be approximated as

$$P \approx \left(\frac{t_1}{t_a}\right)^2 = \left(\frac{t_a t_l t_r}{t_a}\right)^2 = t_l^2 t_r^2. \quad (12)$$

Note that  $t_a$  cancels out in the calculation of  $P$ , and thus the absolute value of  $t_a$  has little effect on  $P$ . Therefore, cloud-free brightness temperatures can be easily approximated employing a transmittance of unity in (9), in which case  $T_{B,O} = \epsilon T_S$ .

Once the high-resolution field of  $P$  had been computed for each simulated rain-rate field, both the rain-rate field and the  $P$  field were spatially averaged. The rain-rate field was averaged using a moving window of  $15\text{ km} \times 15\text{ km}$ , representing the nominal retrieval resolution of the algorithm. The simulated  $P$  values for each TMI channel were spatially averaged using a Gaussian approximation to the effective field of view for that channel. Gaussian random noise with standard deviations of 0.01, 0.02, and 0.02 for the 10.65-, 19.35-, and 37.00-GHz channel, respectively, was then added to  $\mathbf{P}$  in order to reasonably account for errors resulting from the highly simplified nature of the forward model, instrument noise, and similar variables. The above procedure yielded a large ensemble of matched FOV-averaged rain rates  $R$  and attenuation indices  $P_{10}$ ,  $P_{19}$ , and  $P_{37}$ .

### 3) COMPARISONS WITH TMI-DERIVED ATTENUATION INDEX

To evaluate the statistical representativeness of our simulated  $\mathbf{P}$ , we compared the 3D PDF of  $\mathbf{P}$  derived from the simulations with that obtained from 110 actual TMI orbits during 1999 and 2000. Figure 1 compares 2D slices from the 3D distributions for simulated and actual data. Despite the simplicity of the forward model and the utilization of continental radar observations as a proxy for the spatial structure of oceanic rainfall, there is surprisingly strongly qualitative similarity between the two distributions. We can therefore have some confidence in the utility of our simulations for constructing our Bayesian algorithm and for conducting further sensitivity tests.

Three important characteristics of  $\mathbf{P}$  are shown in Fig. 1. First, theoretically, in a homogeneous case of rain cloud, a unique nonlinear relationship in  $\mathbf{P}$  is expected. However, in reality, owing mainly to variable beam filling,  $\mathbf{P}$  exhibits considerable scatter in 3D space. Both observations and simulations show similar magnitudes of this effect. Second,  $P$  may sometimes be slightly greater than 1 in cloud-free cases (but smaller than 1.1 in most cases), because of a combination of instrument noise, errors in water vapor and surface wind speeds, and errors in regression equations. Our analytic models for the conditional distribution will account for this effect. Third, polarization differences at 10.65 GHz of less than 30 K are exceedingly rare in the TMI dataset; correspondingly, very few observed values of  $P_{10}$  are less than 0.4. This observation highlights the fact that rainfall is almost never both horizontally uniform and heavy enough to saturate the 10.65-GHz channel.

## 4. Algorithm basis

As stated in Bayes's theorem, the Bayesian posterior density function is determined by conditional likelihoods that statistically describe physical relationships between the rain rate and microwave signal, and a prior rain-rate distribution that represents our knowledge. Therefore, there are three key elements in our algorithm: the conditional likelihood, the prior distribution, and the estimator interpreting the posterior distribution. In this section, we introduce generic forms to model the prior and conditional distributions. These forms fitting to radar-radiative model simulations will be a basis for further sensitivity tests.

### a. Conditional probability density function

The conditional likelihood  $f(\mathbf{P}|R)$  is a multivariate probability distribution. We used two methods to char-



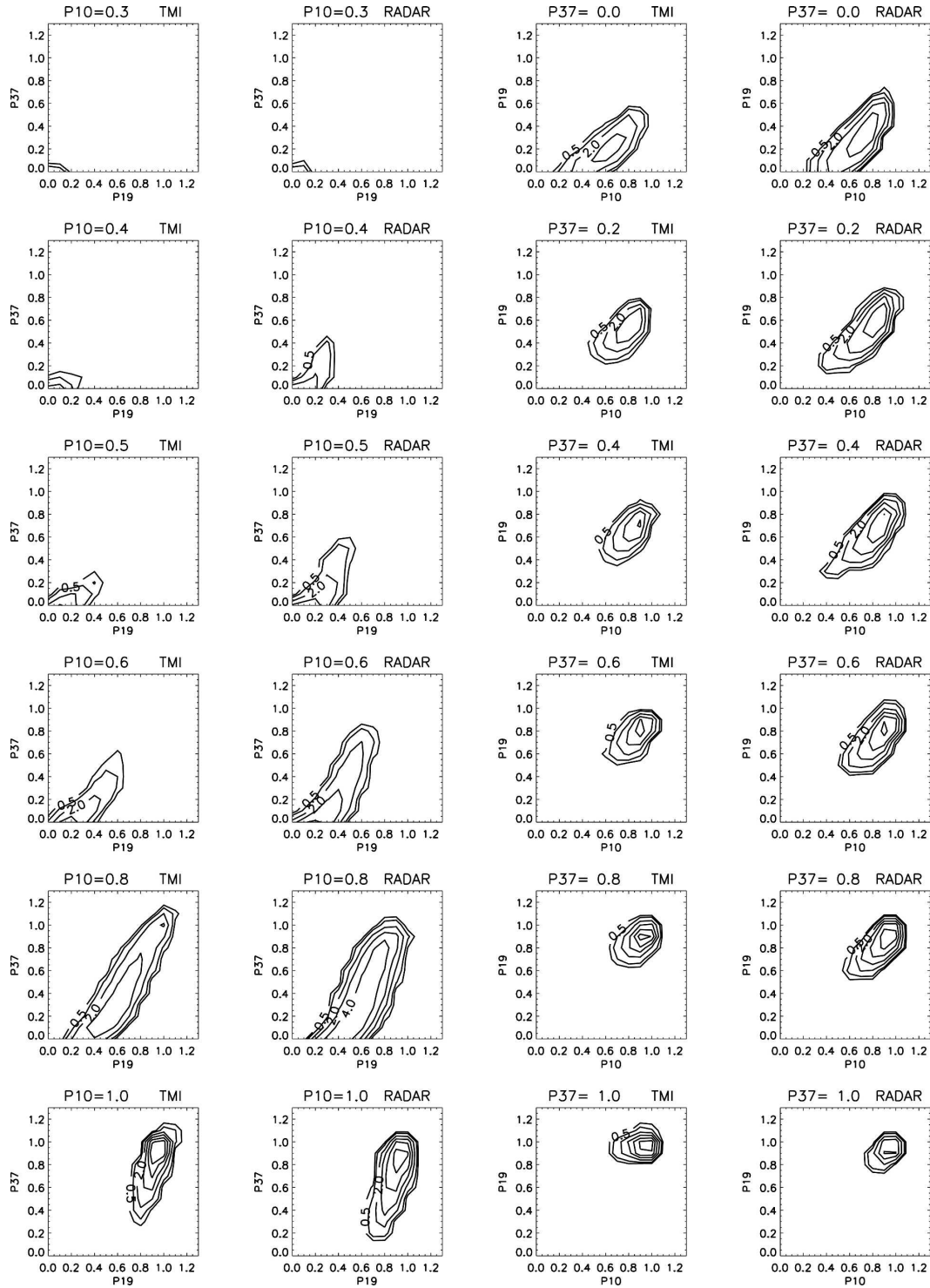


FIG. 1. Contours of the number of pixels based on TMI data (the first and the third columns). Contours are logarithmically spaced; actual value is  $10^x$ , where  $x$  is the contour label;  $x$  are plotted for values of  $[0.5, 1, 2, 3, 4, 5]$ .

acterize the conditional PDF. The first method is to use a covariance matrix to include linear relationships only between rain rate and microwave signature, which is similar to the parameterization of current available

Bayesian algorithms. However, as shown in observations and simulations (Fig. 1), linear properties are not sufficient to approximate the multichannel dependency of microwave signature. Therefore, in the second

method, we took a successive approach to describe the conditional PDF that included linear as well as nonlinear relationships. We will refer to these as “the linear model” and “the nonlinear model,” respectively.

### 1) THE LINEAR MODEL

Similar to a multivariate Gaussian distribution, the conditional PDF between  $\mathbf{P}$  and  $R$  can be written as

$$f(\mathbf{P}|R) \propto P_{10}(a - P_{10})P_{19}(a - P_{19})P_{37}(a - P_{37}) \exp\left[-\frac{1}{2}(\mathbf{P} - \boldsymbol{\mu})\mathbf{C}^{-1}(\mathbf{P} - \boldsymbol{\mu})^T\right]. \quad (13)$$

This closed-form function is essentially a normal distribution in the interior of the interval  $[0, a]$ , but is forced to zero at the boundaries by the term of  $P(a - P)$  for each frequency. Based on observed ranges of actual TMI-derived values  $a$  is chosen to be 1.1;  $\mathbf{C}$  is the covariance matrix, and  $\boldsymbol{\mu}$  is

$$\boldsymbol{\mu} = (\mu_1, \mu_2, \mu_3), \quad \text{where} \quad (14)$$

$$\mu_i = a_{\mu,i} \exp(-b_{\mu,i}R) + c_{\mu,i}, \quad (15)$$

where the subscripts 1, 2, and 3 describe the quantities at 10.65, 19.35, and 37.00 GHz, respectively. Subindex  $i$  is the corresponding channel. Based on the radar-radiative simulations, there parameters can be approximated by Table 2 and

$$\mathbf{C} = \begin{bmatrix} 0.010 & 0.015 & 0.020 \\ 0.015 & 0.040 & 0.045 \\ 0.020 & 0.045 & 0.060 \end{bmatrix}. \quad (16)$$

### 2) THE NONLINEAR MODEL

The more complete physical model is developed to account for the linear as well as nonlinear relations of  $\mathbf{P}$  to rain rate. The distribution of  $\mathbf{P}$  at a given rain rate  $R$  is approached hierarchically:

$$f(\mathbf{P}|R) = f(P_{37}|R)f(P_{19}|P_{37}, R)f(P_{10}|P_{19}, P_{37}, R), \quad (17)$$

TABLE 2. Coefficients of  $a_\mu$ ,  $b_\mu$ , and  $c_\mu$ .

Channel (GHz)	$a_\mu$	$b_\mu$	$c_\mu$
10.65	0.75	0.03	0.30
19.35	1.35	0.05	-0.30
37.00	1.55	0.10	-0.50

where  $f(P_{37}|R)$  is the likelihood of  $P_{37}$  at a given  $R$ ,  $f(P_{19}|P_{37}, R)$  is the PDF of  $P_{19}$  when  $P_{37}$  and  $R$  are fixed, and the  $f(P_{10}|P_{19}, P_{37}, R)$  describes the PDF of  $P_{10}$ , while the other three variables are known. These conditional PDFs, for example, can be approximated as

$$f(P_{37}|R) \propto P_{37}(a - P_{37}) \exp\left[-\frac{1}{2\sigma_3^2}(P_{37} - \mu_3)^2\right]; P_{37} \in [0, a], \quad (18)$$

$$f(P_{19}|P_{37}, R) \propto P_{19}(a - P_{19}) \exp\left[-\frac{1}{2\sigma_2^2}(P_{19} - \mu_2)^2\right]; P_{19} \in [0, a], \quad (19)$$

where  $\mu_2$ ,  $\mu_3$ ,  $\sigma_2$ , and  $\sigma_3$  are all determined by fitting the same radar-radiative model simulations. Complete parameterizations can be found in Chiu (2003).

### b. The prior distribution of rain rate

Surface rain-rate distributions have been commonly parameterized by lognormal functions (Houze and Cheng 1977; Kedem and Chiu 1987; Kedem et al. 1990, 1997; Sauvageot 1994; Nzeukou and Sauvageot 2002), although some observations showed departures from the lognormal distribution (Jameson and Kostinski 1999) and some suggested that rain rates followed gamma distributions (Ison et al. 1971; Swift and Schreuder 1981; Wilks and Eggleston 1992). Because Cho et al. (2004) found that both lognormal and gamma distributions were able to characterize the PDF of rain rates from TRMM data, we used lognormal functions as the prior distribution.

The lognormal density function for the prior distribution is denoted as  $\log N(\mu, \sigma)$  and defined as

$$\log N(r|\mu, \sigma) = \begin{cases} \frac{1}{R\sigma\sqrt{2\pi}} \exp\left[-\frac{1}{2\sigma^2}(\ln R - \mu)^2\right], & R > 0 \\ 0, & R = 0 \end{cases}, \quad (20)$$

where  $\mu$  and  $\sigma$  are the mean and standard deviation ( $\text{mm h}^{-1}$ ) of the variable. These two parameters vary with different rain-rate observation datasets. Therefore, we will evaluate the effect of varying  $(\mu, \sigma)$  on the simulated retrievals.

### c. Estimators of the posterior distribution

When the conditional and prior likelihoods are specified, based on the Bayes theorem [(1)], the posterior distribution can be derived by

$$\pi(R|\mathbf{P}) = \frac{f(\mathbf{P}|R)\pi(R)}{\int f(\mathbf{P}|R)\pi(R) dR}. \quad (21)$$

Integrations with respect to rain rate in the four-dimensional space were performed numerically. Once the posterior distribution is known, the two most common estimators were taken: the mean and the maximum likelihood estimate of the posterior probability distribution, denoted as MEAN and MLE, respectively. The corresponding Bayesian estimates are stored in a three-dimensional lookup table for each  $\mathbf{P}$  for single-pixel retrievals.

## 5. Sensitivity tests

### a. Experiment design

A number of experiments are designed for the sensitivity test by various combinations of the prior and conditional likelihoods (summarized in Table 3). The retrieval target was produced from a random number generator that followed all conditional PDFs of the nonlinear model [(17)–(19)]. Because one of our purposes for the sensitivity tests is to better understand the behavior of retrieval at higher rain rates, we generated this dataset along with the prior distribution  $\log N(0, 2)$  to prevent a scarcity of high rain intensity.

The control run (R0) is the experiment in which the Bayesian retrieval method uses exactly the same conditional and prior PDFs with the retrieval target. An analysis of this control experiment can provide insight into the inherent uncertainty of the retrieval, because each PDF is perfect and no assumption is made in the algorithm. Furthermore, by comparing the control run with other experiments, the sensitivity of the algorithm to the prior distributions of rain rate can be evaluated by experiments R1 and R2, while R3 and R4 aim to understand the sensitivity to the conditional likelihoods. In experiment R3, we used a different parameterization for  $f(P_{19}|P_{37}, R)$  to investigate the sensitivity of the algorithm to various explicit functions. Experiment R4 applies the  $\mathbf{P}$ – $R$  relationships of the linear model (i.e., covariance matrix form) into the algorithm. This experiment is vital because it evaluates the adequacy of simple assumptions of the conditional PDFs in the retrieval algorithm, when in fact the dataset has a much larger degree of complexity.

### b. Intrinsic uncertainty of the algorithm

As we have emphasized through this paper, a key property of the Bayesian algorithm is its ability to ob-

TABLE 3. Information of designed experiments in sensitivity tests, including the experiment identifier (ID), the training dataset, and the specifications of the prior and conditional likelihoods applied to the Bayesian algorithm.

Expt ID	$\pi(R)$	Physical model
R0	$\log N(0, 2)$	Nonlinear model from (17)–(19)
R1	$\log N(0, 1)$	Nonlinear model from (17)–(19)
R2	Uniform [0, 100]	Nonlinear model from (17)–(19)
R3	$\log N(0, 2)$	Different parameterizations in (19)
R4	$\log N(0, 2)$	Linear model from (13)–(16)

tain complete posterior PDFs of retrieved rain rates. Based on the complete posterior distribution, a probability statement can be made about the realization of the retrieval. This advantage allows us to assess intrinsic uncertainties of the retrieval, when the ideal physical model and exact prior distribution are applied to the algorithm.

Figure 2 shows examples of the posterior distributions from experiment R0. Some posterior distributions have a single maximum over the entire rain-rate range, but some have two. A single maximum expresses the situation that a given observation vector  $\mathbf{P}$  provides unambiguous information about the most likely rain rate when both physical relationships and prior knowledge are taken into account. A bimodal distribution implies that two distinct rain intensities are of comparable likelihood. The peak on the left indicates a scene of widespread stratiform precipitation associated with a smaller rain rate, while the second peak suggests the possibility of a strong convective cell within that  $15 \text{ km} \times 15 \text{ km}$  area. Based on the posterior PDFs of Fig. 2b, the MLE retrieval can increase from 5 to  $60 \text{ mm h}^{-1}$  if  $P_{10}$  decreases from 0.64 to 0.60 and  $P_{19}$  and  $P_{37}$  remain the same. However, in reality, this magnitude of the change in  $P$  value may not relate to a dramatic change of rain intensity of the scene, but rather arises from the variations of the instrument noise, atmospheric condition, and/or the calculations of brightness temperatures. Therefore, caution should be exercised in these cases when single-pixel retrievals are of interest. Such cases may be easily detected via their larger associated standard deviations.

Performance of the Bayesian algorithm at different rain-rate ranges for experiment R0 is demonstrated from the histogram of retrieved rain rates (as shown in Fig. 3). The title for each subplot is made of three components. The first component RR indicates the specific range of rain rates, where the retrieved rain intensity is drawn if its corresponding true rain rate in the training dataset is in this range. The second component is the

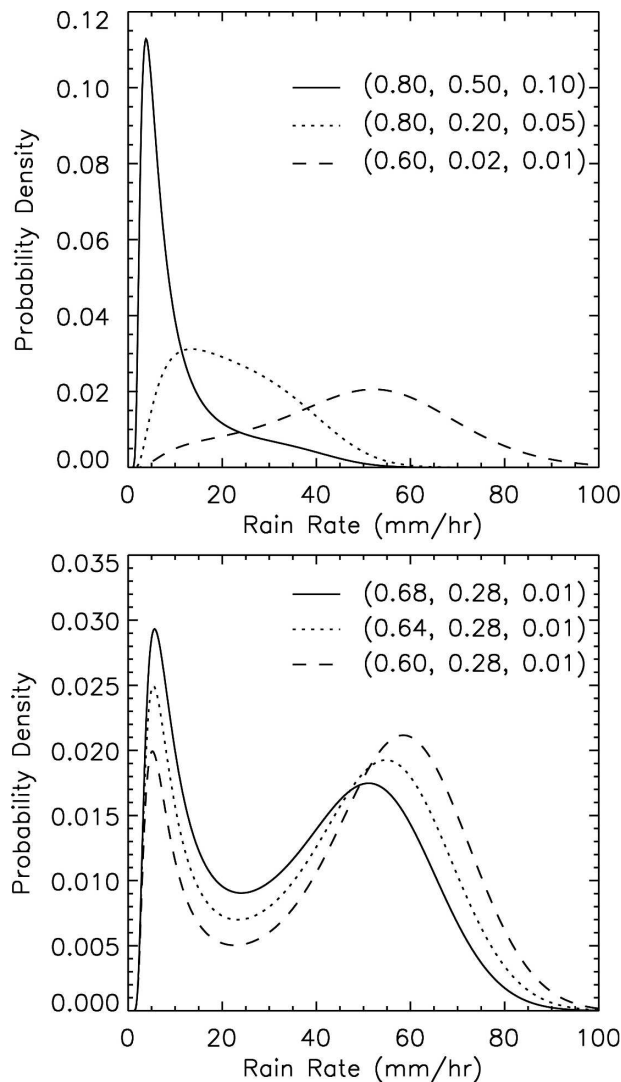


FIG. 2. Examples of derived posterior rain-rate distributions at some given  $P$  vectors in experiment R0. The observation vector ( $P_{10}$ ,  $P_{19}$ ,  $P_{37}$ ) is presented by the three numbers in parentheses.

sample size of the histogram. The third component, MEAN or MLE, describes the estimate used to interpret the posterior distribution. The pair of the numbers on the upper-right corner in each subplot is the mean and standard deviation of the histogram, while the percentage is the proportion of the retrieved rain rates that are in the same range as the actual rainfall intensities with respect to the whole histogram. Note that for the true range RR lower than  $30 \text{ mm h}^{-1}$ , the histogram is plotted in a logarithmic scale.

Results from experiment R0 using MEAN estimates suggest that the Bayesian algorithm is able to retrieve the light rain rate very well. For the moderate intensity ( $7\text{--}15 \text{ mm h}^{-1}$ ), the retrieval algorithm captures 46% of the data points, and the mean value is about right. The

algorithm tends to underestimate the rain rates when the actual intensity in training data increases to a heavier range. Meanwhile, the associated standard deviation of the histogram starts to increase as well. Even so, the retrievals still encompass 30% data in the true range. For the extremely large rain rate (greater than  $75 \text{ mm h}^{-1}$ ), there are 42% of data in the correct rain range, and the mode of the histogram falls within the true range. In this control experiment, the Bayesian algorithm shows the ability to retrieve rain intensity over all ranges, even for the case with extremely heavy precipitation.

The histogram of MLE retrievals for experiment R0 is shown in Fig. 4. Results from the light rain regime demonstrate a satisfactory performance. However, the underestimation for intermediate intensities ( $4\text{--}30 \text{ mm h}^{-1}$ ) is significant. Moreover, there are two distinct modes in the histogram when the true range RR goes up greater than  $30 \text{ mm h}^{-1}$ . The one associated with a lower rainfall rate dominates in the RR range of  $[30, 75] \text{ mm h}^{-1}$ , and causes some retrievals at least  $20 \text{ mm h}^{-1}$  smaller than the true rain intensity. The other mode becomes dominant under the extremely heavy precipitation, yielding 40% of the data points in the correct range.

In short, experiment R0 has demonstrated the retrieval ability of the Bayesian algorithm over various rain-rate ranges when the prior and conditional likelihoods are both idealized. The single-pixel retrieved rain rates might be associated with a bias because of the inherent uncertainty in the physical relationships and the interpretation using MEAN and MLE. The inherent uncertainty might be reduced via the inclusion of additional information concerning other atmospheric or microwave variables.

### c. Sensitivity to the prior knowledge

Analyses of experiments R1 and R2 demonstrate how retrieved rain rates change to various specifications of the prior distribution when the physical model remains the same. In comparison with the control prior density function, the prior distribution in experiment R1,  $\log N(0, 1)$ , has relatively smaller probabilities at very light rain rates and beyond  $5 \text{ mm h}^{-1}$ . This property of the prior PDF leads the algorithm to retrieve reasonably for the true intensities between  $0.2$  and  $7 \text{ mm h}^{-1}$  from both MEAN and MLE estimates. However, the smaller probability of the prior PDF at higher rain rates obviously limits the ability of the algorithm to retrieve heavy precipitation as shown in Fig. 5. Note that we also conducted other experiments changing  $\mu$  and  $\sigma$  by 10% in prior PDFs, and found that slight



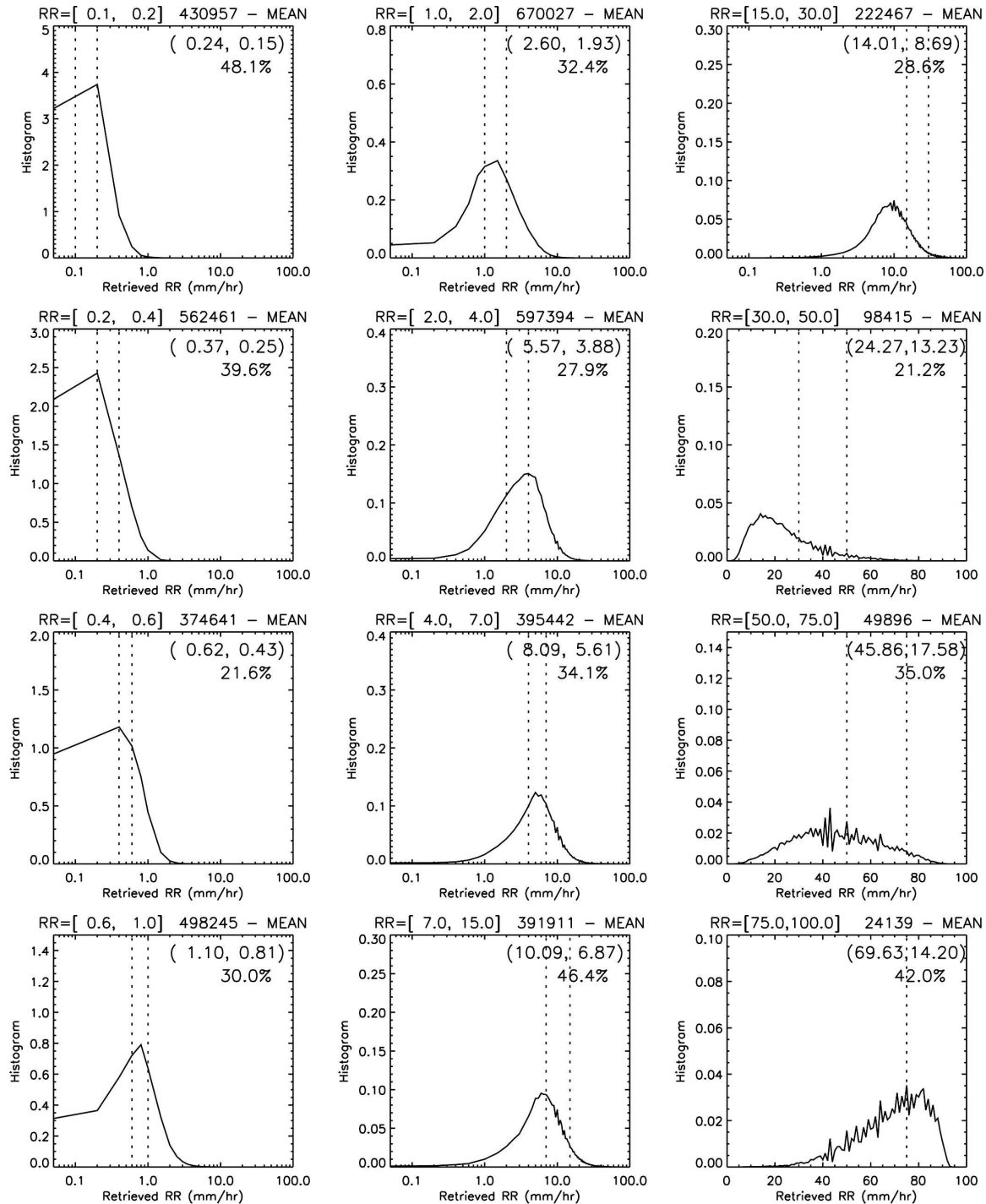


FIG. 3. Histograms of retrievals at different rain-rate ranges for experiment R0. Titles contain information about range of true values of RR, sample size, and the estimator. Numbers in parentheses are the mean and standard deviation of the histogram. Percentages are the fractions of retrieved rain rates located in the correct range.

variations of the prior distribution had no significant effects on the Bayesian algorithm.

A noninformative prior distribution is used in experiment R2, which assigns equal weight to all values over

the parameter space. Based on Bayes's theorem, it is clear that the posterior probability density is now proportional to the likelihood represented only by the data in this experiment, and thus the retrieval is dominated

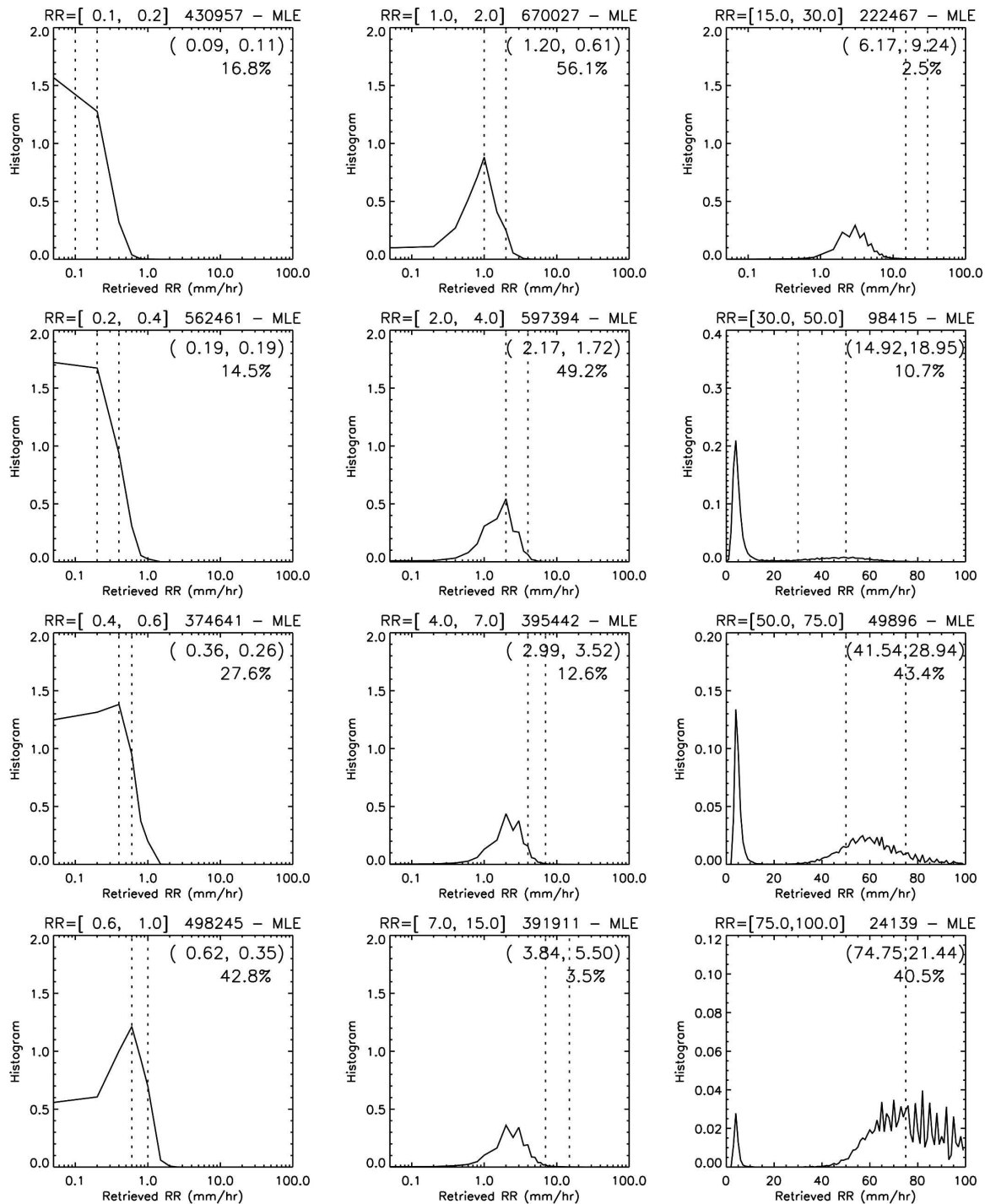


FIG. 4. Same as Fig. 3, but using MLE estimations.

by the behavior of the physical model. Results demonstrate that a uniform prior PDF yields much higher retrieved rain rates by 7–15 mm h<sup>-1</sup> in light and moderate rain situations (not shown). For the true range with heavier rain rates, experiment R2 captures around

50% of the data points in the correct range. Because experiment R2 only includes the information of data with no prior knowledge, it is suggested that the **P** we used is sufficient to reflect the rainfall signal, even in heavy precipitating systems.



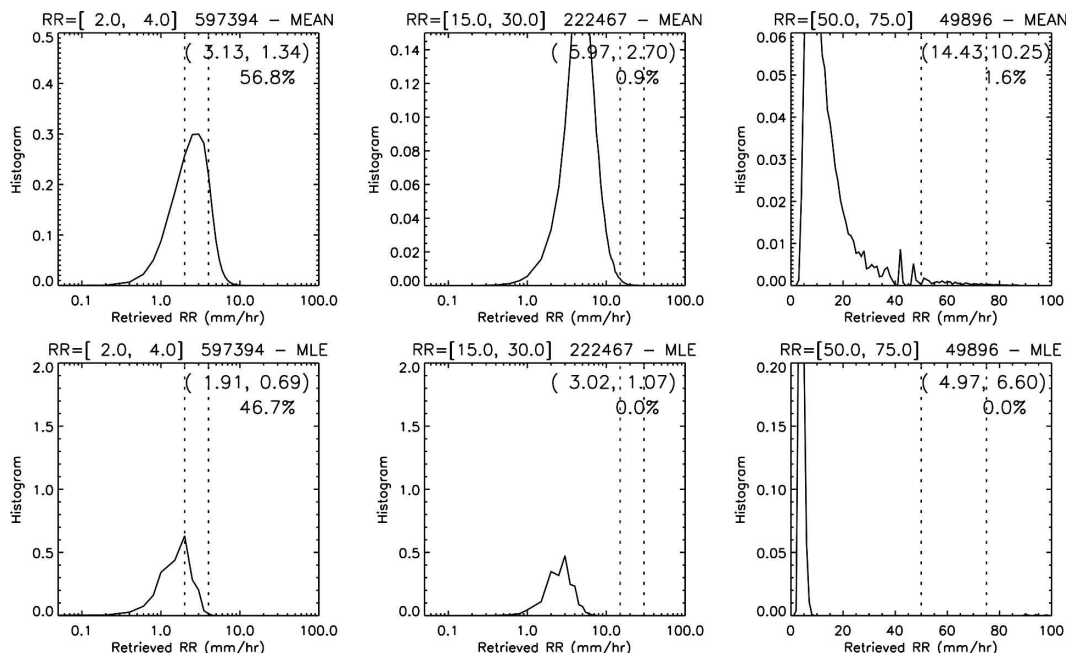


FIG. 5. Retrieval histogram of experiment R1 at rain-rate ranges of [2, 4], [15, 30], and [50, 75]  $\text{mm h}^{-1}$  for (top) MEAN and (bottom) MLE.

In summary, the prior rain-rate distribution plays a crucial role in the Bayesian algorithm retrieval, because the characteristics of the prior PDFs determine the retrieval ability and bias at different rain-rate ranges. However, the Bayesian retrieval is not sensitive to slight fluctuations of the parameters used in the prior PDFs. Therefore, when the prior rain-rate distribution is applied reasonably, the Bayesian algorithm is still robust.

#### d. Sensitivity to the conditional distribution

This section advances our understanding of the sensitivity of Bayesian retrievals to the characterization of conditional likelihoods that provide statistical and physical relationships between  $\mathbf{P}$  and  $R$ . First, we attempted to understand whether different explicit functions characterizing conditional distributions would have a substantial impact on retrievals. In experiments R0 and R3, the conditional PDFs were both derived from the same radar-radiative simulations, and they presented similar relationships between  $\mathbf{P}$  and  $R$ . As a result, experiment R3 yields consistent retrievals with experiment R0 for both MEAN and MLE estimates (not shown). It indicates that the specifications of the conditional distributions are not critical if the  $P$ - $R$  relationships represented by those PDFs are not far from reality.

Second, we attempted to evaluate the adequacy of

using simplified conditional PDFs to represent more complicated behaviors of data by using experiment R4. Figure 6 depicts the microwave multichannel relationships represented in experiment R0 (upper panel) and R4 (bottom panel). These relationships demonstrate similar patterns, including the orientation and spread of the contours. However apparently, the locations of the maximum likelihoods are shifted to lower  $P$  values in experiment R4.

Histograms of retrievals from the MEAN estimates of experiment R4 are shown in Fig. 7 (results of MLE are not shown because of similar responses). In general, for both MEAN and MLE estimates, the use of a linear covariance matrix to describe conditional likelihoods significantly overestimates rain rates, and the variations of the retrieval histograms are almost twice than those of the control experiment R0. More specifically, for very light rain rates, R4 only produces 0.1% of the data points in correct ranges, while the control run successfully retrieves almost half of data. The positive bias becomes more significant when true rain rates are of a moderate intensity. Under the condition that the true rain rates are only 2–15  $\text{mm h}^{-1}$ , some retrievals from R4 are even greater than 50  $\text{mm h}^{-1}$ . The large variation in retrieved intensity is also seen in the case of heavy precipitation.

One should not conclude that a simplified physical model is always unsuitable for the use of a Bayesian

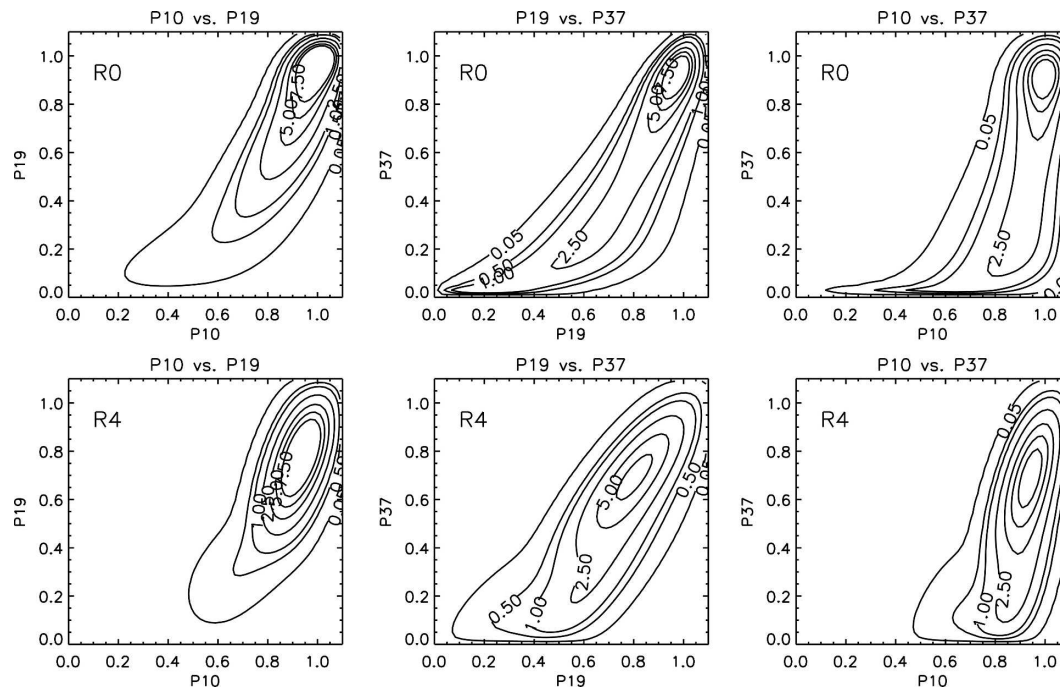


FIG. 6. Joint PDFs of the  $\mathbf{P}$  vector for experiment (top) R0 and (bottom) R4. Contours are plotted for [0.05, 0.5, 1.0, 2.5, 5.0, 7.5, 10].

algorithm, because considerable differences exist in the multichannel relationships between the retrieval target dataset and the applied physical model for experiment R4. The retrieval bias may be reduced if the simple physical model is improved or tuned to be closer to the training dataset. However, we must note that the covariance matrix facilitating the linear model was estimated from the same radar-radiative simulations that were used in the explicit functional model. Therefore, it is clear that the simplified physical model cannot explain all of data behaviors, and this deficiency will lead to a significant bias in some ranges of rain rates.

## 6. Applications to TMI data

This section provides applications of our new Bayesian algorithm to TMI data, including implements and validations against PR data. In previous sections, we trained our algorithm with radar-radiative simulations. In an attempt to construct an algorithm based on calibrate precipitation measurements, we used the same framework here, but the prior and conditional PDFs were adjusted based on actual PR and TMI matchups.

### a. PR–TMI matchup data

Since there is no long-term/wide-area dense rain gauge network or other reliable data to provide true

rainfall intensity over the ocean, we used near-surface rain rates of the TRMM standard product 2A25 (retrieval from the PR) to develop and validate our TMI Bayesian retrieval algorithm. The 2A25 PR products provide retrieved rain rates with 4-km resolution. Because our retrievals represented rain intensity at a 15-km resolution, PR surface rain rates were averaged using a Gaussian weighting function and interpolated to the locations of TMI pixels. For convenience, the averaged rain-rate estimates are hereinafter referred to as PR rain rates. Note that PR reflectivity measurements can suffer from sidelobe contamination when the main beam of the PR is off nadir, and the resulting errors would propagate into rain-rate estimates. To minimize the likely impact of these errors, only matchups between TMI observations and near-nadir PR estimates are utilized.

The probability distribution of near-nadir  $15 \text{ km} \times 15 \text{ km}$  PR rain rates from data of January, April, July, and October 1998 was found to be comparable to (20). Because of the minimum detectable threshold ( $\sim 17 \text{ dBZ}$ ) of PR reflectivity, we applied a cutoff of  $0.04 \text{ mm h}^{-1}$  to yield parameters ( $\mu$ ,  $\sigma$ ) of  $(-2.8, 2.0)$ . In addition, we used 2 months of PR–TMI matchups (January and July 1998) to adjust conditional PDFs of our Bayesian algorithms. Detailed parameterizations are given in Chiu (2003).

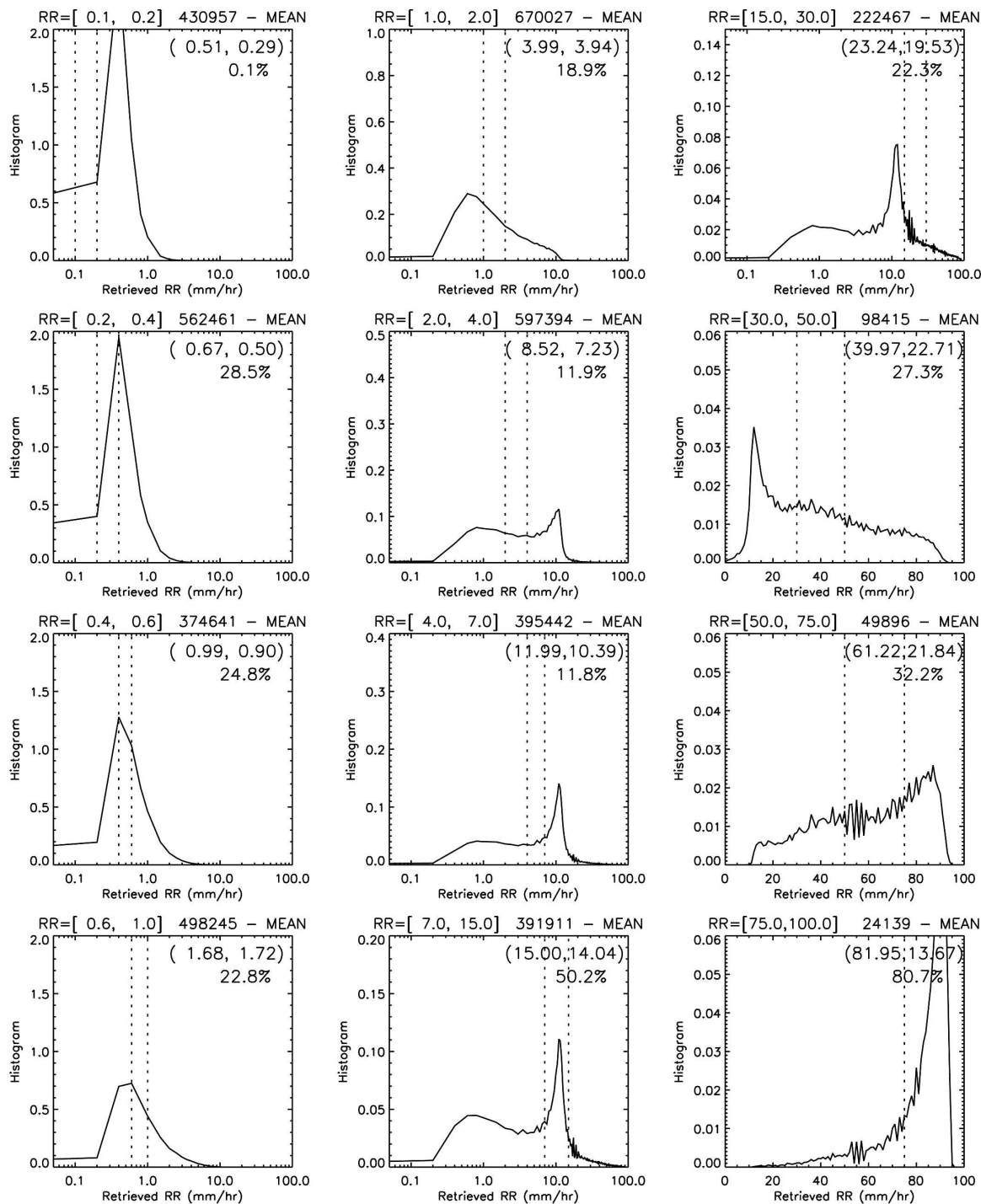


FIG. 7. Same as Fig. 3, but for experiment R4.

### b. Validation datasets

We used a number of cases to evaluate the overall performance for all algorithms. In addition to looking at the quasi-global performance, we also considered specific classes of precipitating systems. These

included tropical cyclones, frontal rainbands in extratropical cyclones, and some scattered strong convection cells. The purpose behind the selection of these cases is to evaluate the degree to which algorithm performance depends on the nature of the precipitation cloud system under consideration, especially

TABLE 4. Bias, RMSD (both: mm h<sup>-1</sup>), and correlation coefficients (Corr) for each algorithm and each validation dataset.

	Orbit 336			Bauer's cases			April 1998		
	Bias	RMSD	Corr	Bias	RMSD	Corr	Bias	RMSD	Corr
GPROF	-0.22	2.68	0.88	-0.22	1.64	0.76	-0.21	1.18	0.78
Linear model	-0.29	2.71	0.88	0.00	1.58	0.78	-0.08	1.09	0.81
Bayesian-MEAN	0.00	2.89	0.85	0.08	1.84	0.71	0.03	1.26	0.78
Bayesian-MLE	-1.04	3.75	0.85	-0.29	1.80	0.74	-0.01	1.21	0.75

when the latter is, in some sense, atypical of global precipitation.

### 1) INDIVIDUAL TEST CASES

A typhoon case from TMI orbit number 336 as well as 12 oceanic cases from Bauer et al. (2001) were selected as individual test cases for retrieved rain rates. As before, the so-called true rain rate in the validation dataset is obtained from the coincident PR 15 km × 15 km averaged rain rate.

### 2) APRIL 1998 PR-TMI GLOBAL MATCHUP DATA

For quasi-global validation purposes, 118 orbit files in April 1998 were randomly selected to validate the overall performance of all algorithms. Note that our Bayesian retrieval algorithm was derived from the data of January and July in 1998, and therefore, the PR-TMI matchup data of April is independent for the purposes of this validation.

### c. Benchmark algorithms

Two benchmark algorithms are utilized in this study to provide intercomparisons for the purpose of validations. One benchmark algorithm is the GPROF, which is the official algorithm for TMI data (Kummerow et al. 1996, 2001; Olson et al. 1996, 2006). This algorithm introduced a database to represent the presumed probability distribution of rain rate and cloud profiles. Cloud profiles with microwave signatures that are close to satellite observations are picked from the database as candidates. The selected candidates are then averaged to yield the best surface rain rate and precipitation structure for each pixel, based on the relative occurrence of each cloud profile in the database.

The other benchmark algorithm is a linear regression model developed from PR-TMI matchup data in January and July 1998. Regression variables include the  $P_{10}$ ,  $P_{19}$ ,  $P_{37}$ , and scatter index at 37 and 85 GHz ( $S_{37}$  and  $S_{85}$ ; Petty 1994a). The linear model is formulated as follows:

$$\begin{aligned}
 P_{10}^* &= \frac{P_{10}^{\lambda_1} - 1}{\lambda_1}, \lambda_1 = -0.8, \\
 P_{19}^* &= \frac{P_{19}^{\lambda_2} - 1}{\lambda_2}, \lambda_2 = -0.3, \\
 P_{37}^* &= \frac{P_{37}^{\lambda_3} - 1}{\lambda_3}, \lambda_3 = -0.7, \text{ and} \\
 R &= 0.201 + 4.10P_{10}^* - 4.831P_{19}^* + 0.182P_{37}^* \\
 &\quad + 0.110S_{37} + 0.017S_{85} + 0.810P_{10}^*P_{19}^* \\
 &\quad + 0.960P_{10}^*P_{37}^* - 0.234P_{19}^*P_{37}^* + 0.117P_{10}^*P_{19}^*P_{37}^*,
 \end{aligned}
 \tag{22}$$

where  $R$  is retrieved rain rate (mm h<sup>-1</sup>), and the asterisk symbol represents transformed variables. In this model, all pixels were retrieved without rain screening. Therefore, some constraints were needed for calculated rain-rate fields in order to exclude unrealistic precipitation. It is assumed that the pixel is not rainy when its retrieved rain intensity is smaller than 0.5 mm h<sup>-1</sup>.

The linear algorithm may be regarded as the least sophisticated of the algorithms, in that it does not account for either nonlinearity in the relationship between  $R$  and the microwave observables or the highly non-Gaussian distributions of these variables. Hence, differences in the performance of this algorithm from the other algorithms may be regarded as a measure of the relative importance of these characteristics.

These two benchmark algorithms provide single-pixel retrieved rain rates only. To compare our retrievals with them, we used MEAN and MLE to represent the “best” retrieved rain rates, denoted as Bayesian-MEAN and Bayesian-MLE, respectively.

### d. Validation metrics

There are several common validation statistics employed to characterize differences between retrieved estimates and true values. Of these, the difference between the mean [or mean bias (bias)], the root-mean-squared difference (RMSD), and the linear correlation coefficient are the most commonly used. It bears emphasizing that no performance statistic for any single



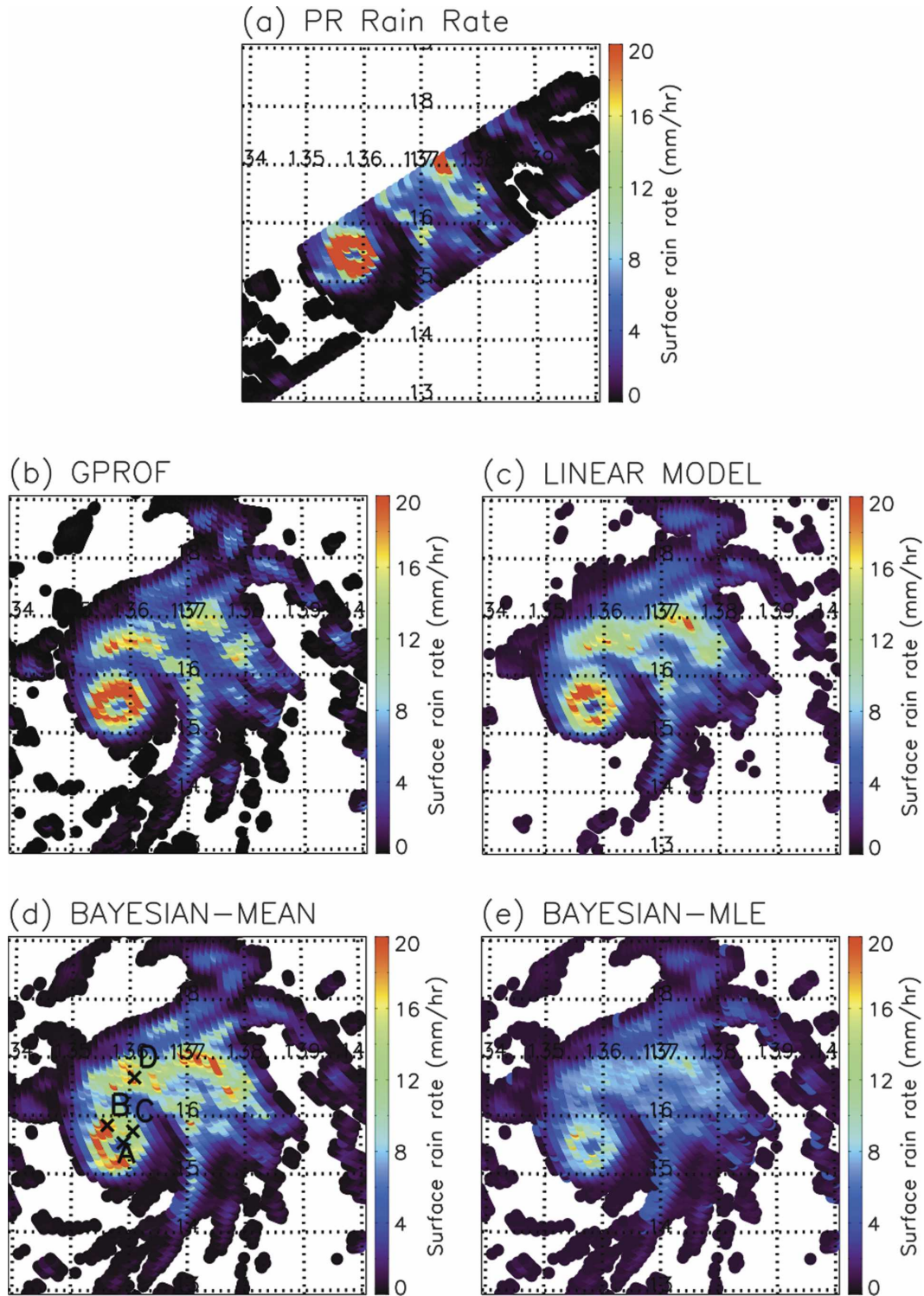


FIG. 8. (a) PR interpolated rain rates with a 15-km resolution for TMI orbit 336. Retrieved rain rate ( $\text{mm h}^{-1}$ ) from (b) GPROF, (c) the linear model algorithm, (d) Bayesian-MEAN, and (e) Bayesian-MLE models for TMI orbit 336.

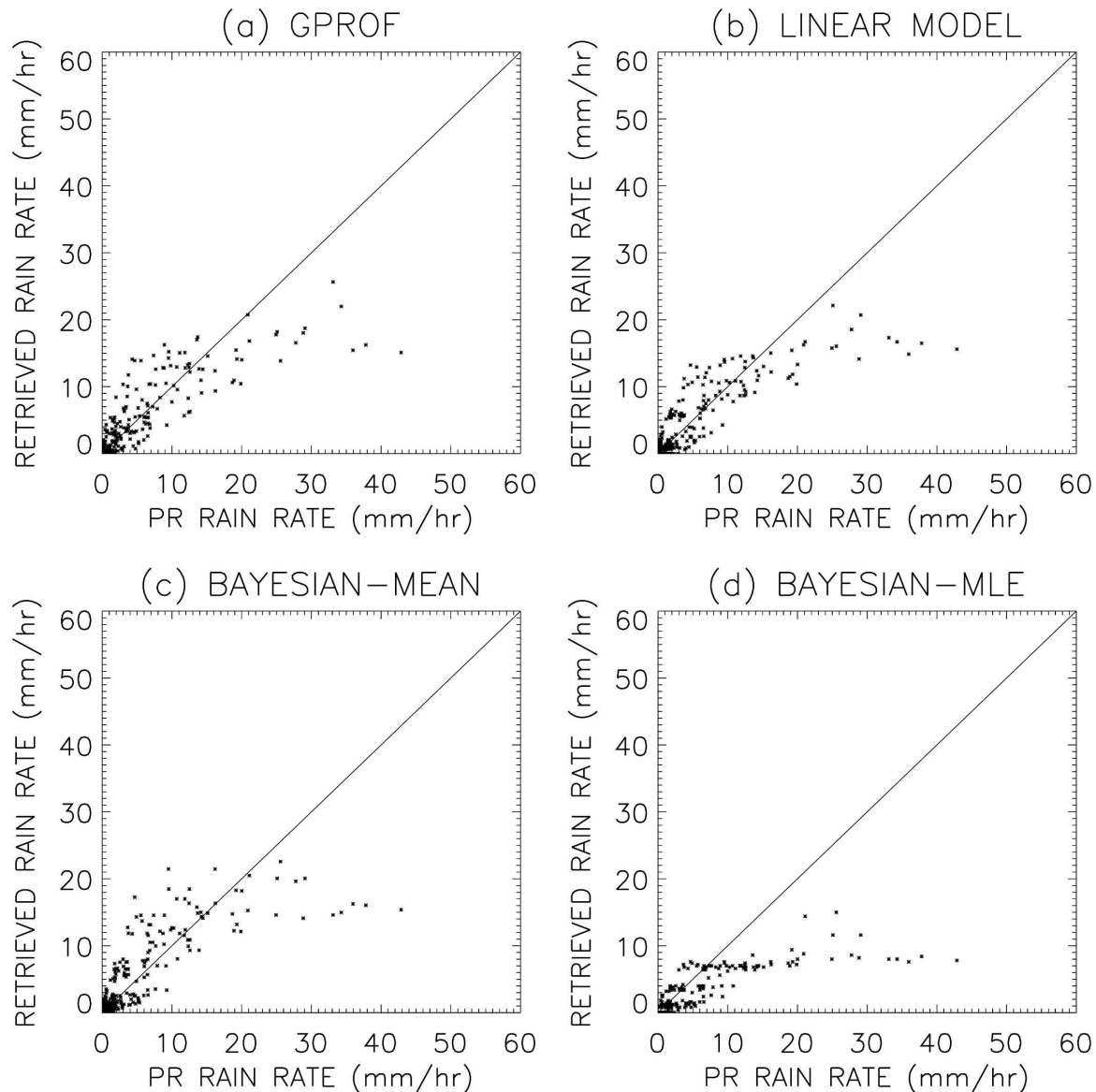


FIG. 9. Scatterplot of retrieved rain rate vs PR rain rate for all algorithms for TMI orbit 336.

algorithm is meaningful when considered in isolation, because it invariably depends on the statistical and physical properties of the validation dataset. We can therefore assess the “goodness” of any outcome only by comparing the results of several competing algorithms applied to identical datasets.

The linear correlation coefficient represents the strength of the linear relationship between observations and retrievals. Unlike either bias or RMSD, it is not affected by linear systematic errors in either the validation data or the retrievals and it is therefore a better measure of intrinsic (or potential) algorithm performance at discriminating between high and low rain rates. However, a systematic *nonlinear* bias, though po-

tentially correctable, will adversely affect the correlation coefficient and therefore give a misleading indication of intrinsic algorithm skill.

A drawback to any of the traditional metrics is that they do not distinguish between performances at high and low rain-rate values; moreover, they do not necessarily distinguish between systematic errors resulting from correctable nonlinearities in an algorithm’s response and retrieval errors of a more random (and therefore noncorrectable) nature. We therefore also employ an adaptation of the Heidke skill score (HSS) proposed by Conner and Petty (1998). They specified separate rain-rate thresholds  $R_v$  and  $R_r$  for the validation data and for the retrievals, respectively, and al-



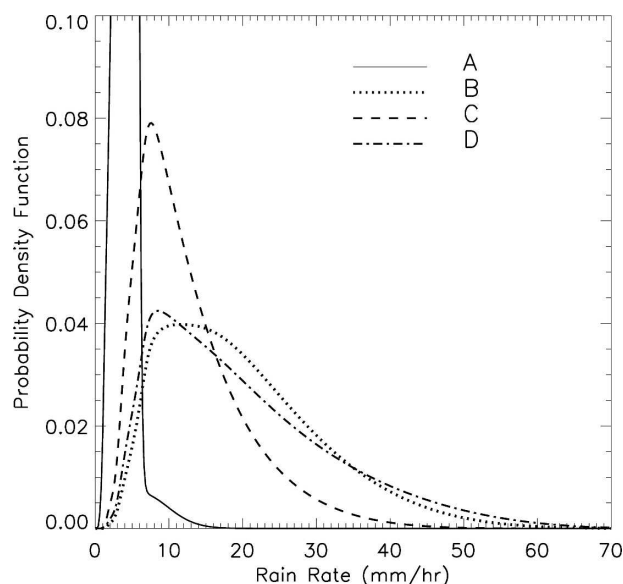


FIG. 10. Posterior PDFs of retrieved rain rates at locations A, B, C, and D that are marked in Fig. 8d.

lowed these to vary independently of one another. The HSS may then be computed and plotted as a continuous bivariate function of the two thresholds. One may then identify those combinations of the two thresholds that maximize the skill score. *The maximum skill found for any given value of  $R_v$  is independent of any calibration bias (linear or nonlinear) in the retrievals.* This method therefore offers a way of characterizing the intrinsic performance of an algorithm at discriminating between high and low (or zero) rain rates, independent of any biases, while also allowing the presence of any such biases to be inferred via the relationship between  $R_v$  and  $R_r$ , which maximizes the skill score.

### e. Results

The performance of all algorithms as measured using conventional validation statistics (bias, root-mean-square error, and correlation coefficient) are summarized in Table 4. For the purposes of this study, the outcome is deemed satisfactory if the performance of our Bayesian algorithm is found to be comparable to that of other algorithms, given that ours has the added advantage of producing posterior PDFs of surface rain rates.

#### 1) TYPHOON CASE

Table 4 shows that the Bayesian-MEAN has a zero bias, a comparable correlation coefficient with GPROF and the linear model, and a slightly larger RMSD for TMI orbit 336. To obtain a direct sense of how different the retrieval from each algorithm behaves, PR and algorithm-retrieved rain rates are mapped in Fig. 8.

Qualitatively, all algorithms are able to retrieve the eye, two separate rainbands, and the overall cyclonic structure of the typhoon. Quantitatively, most algorithms produce rain-rate intensities that are of a similar magnitude to the PR interpolated data. A scatterplot of retrieval versus PR rain rate (Fig. 9) also demonstrates good agreements for all algorithms, though underestimations are seen when rain rates exceed  $30 \text{ mm h}^{-1}$ . In addition, the dynamic retrieval range in the Bayesian-MLE algorithm is around  $10 \text{ mm h}^{-1}$  in this case, which is much smaller than that derived from the posterior mean. This deficiency leads to a significant negative bias in Bayesian-MLE retrievals (Table 4).

Figure 10 illustrates posterior PDFs for points A–D that are marked in Fig. 8d. Point A is located around the eye of the typhoon, and has a narrow spectrum and distinct peak at a smaller rain rate. Points B and C are on the different sides of the wall. Their PDFs show that point B has a heavier tail and thus yields a much larger mean rain rate than that of point C. Point D is located in the one of spiral rainbands. Its associated posterior PDF has a heavy tail as well, and is highly skewed to the right.

#### 2) BAUER'S 12 OCEANIC CASES

For 12 oceanic cases, retrievals from the Bayesian-MEAN algorithm are associated with a bias of only  $0.08 \text{ mm h}^{-1}$  (Table 4), but have a larger root-mean-square error and a smaller correlation coefficient, implying the lack of retrieval ability for heavy rain rates. The linear model has zero bias and the largest correlation coefficient here. The Bayesian-MLE algorithm has a comparable performance with GPROF for these cases.

Figure 11 shows contours of two-dimensional HSS of each algorithm, and indicates that the highest skill scores occur in the range of  $0\text{--}10 \text{ mm h}^{-1}$  for all algorithms. For any given validation rain-rate threshold  $R_v$ , the value of the algorithm rain-rate threshold  $R_r$  can be identified for which the HSS is maximized. We may refer to this as the optimized rain-rate threshold  $R_{\text{opt}}$  for that value of  $R_v$ . Two additional useful types of plots follow from this definition. One is a plot of the  $R_{\text{opt}}$  versus  $R_v$ , which is indicative of apparent bias, relative to the validation data. The other is the plot of maximum HSS (i.e., the skill score computed at  $R_{\text{opt}}$ ) versus  $R_v$ , which represents the intrinsic (bias independent) discrimination ability of the algorithm with respect to rain rates exceeding  $R_v$ .

Figure 12 depicts the relationship between  $R_{\text{opt}}$  and  $R_v$  for the ensemble of 12 overpasses. The linear relations revealed in plots demonstrate that most algorithms, especially the Bayesian-MEAN model, offer good agreement with PR data when true rain rates are

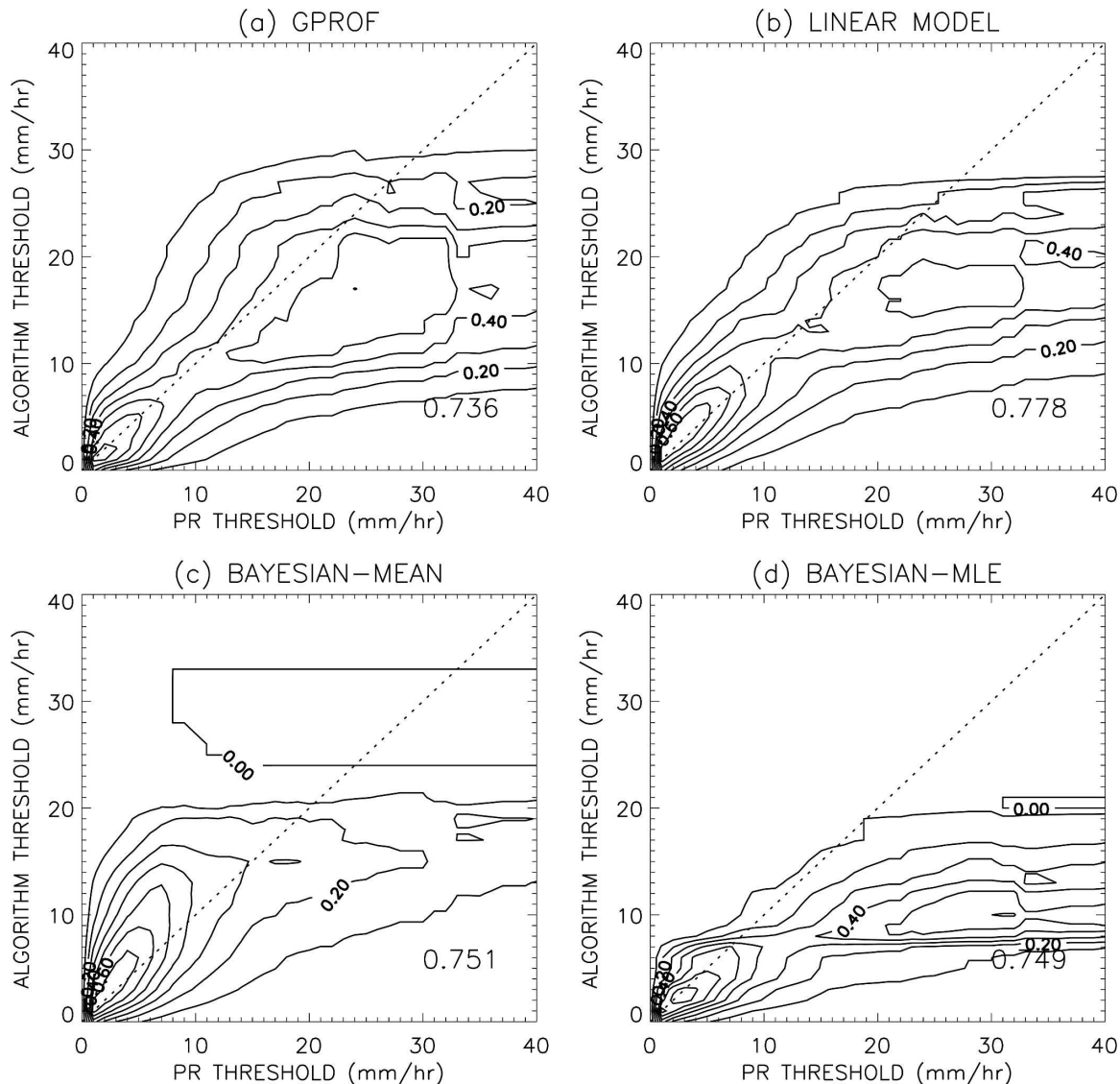


FIG. 11. 2D distribution of HSS for the 12 selected cases from the Bauer et al. (2001). Retrieval algorithms are (a) GPROF, (b) the linear model, (c) Bayesian-MEAN, and (d) Bayesian-MLE. The value noted in the bottom-right corner of each plot indicates the highest HSS of the algorithm. Contours are plotted with an interval of 0.1.

less than  $20 \text{ mm h}^{-1}$ . The degradation at a higher rain rate in our Bayesian algorithm originates from insufficient data samples at a higher rain rate, and the resulting poor fit to the data when we specified our conditional likelihoods. Figure 13 shows the maximum Heidke skill score versus  $R_v$  for this dataset, and all algorithms have comparable discrimination abilities. Because the proportion of the number of hits to the total data points in the contingency table for all algorithms drops dramatically (to less than 1%), the maximum HSS might not be statistically meaningful when the true rain rate is above  $10 \text{ mm h}^{-1}$ . Therefore, we only show the maximum HSS for rain rates up to  $10 \text{ mm h}^{-1}$ .

### 3) APRIL 1998

In the randomly selected cases in April 1998, our Bayesian retrieval algorithms show the smallest bias and a comparable correlation coefficient with that of GPROF. The linear model has the best correlation with PR, but is associated with a negative bias. HSS analysis reveals satisfactory performance of our Bayesian algorithms (figures not shown).

## 7. Summary and discussion

This paper has introduced a new Bayesian retrieval algorithm that provides continuous posterior probabil-

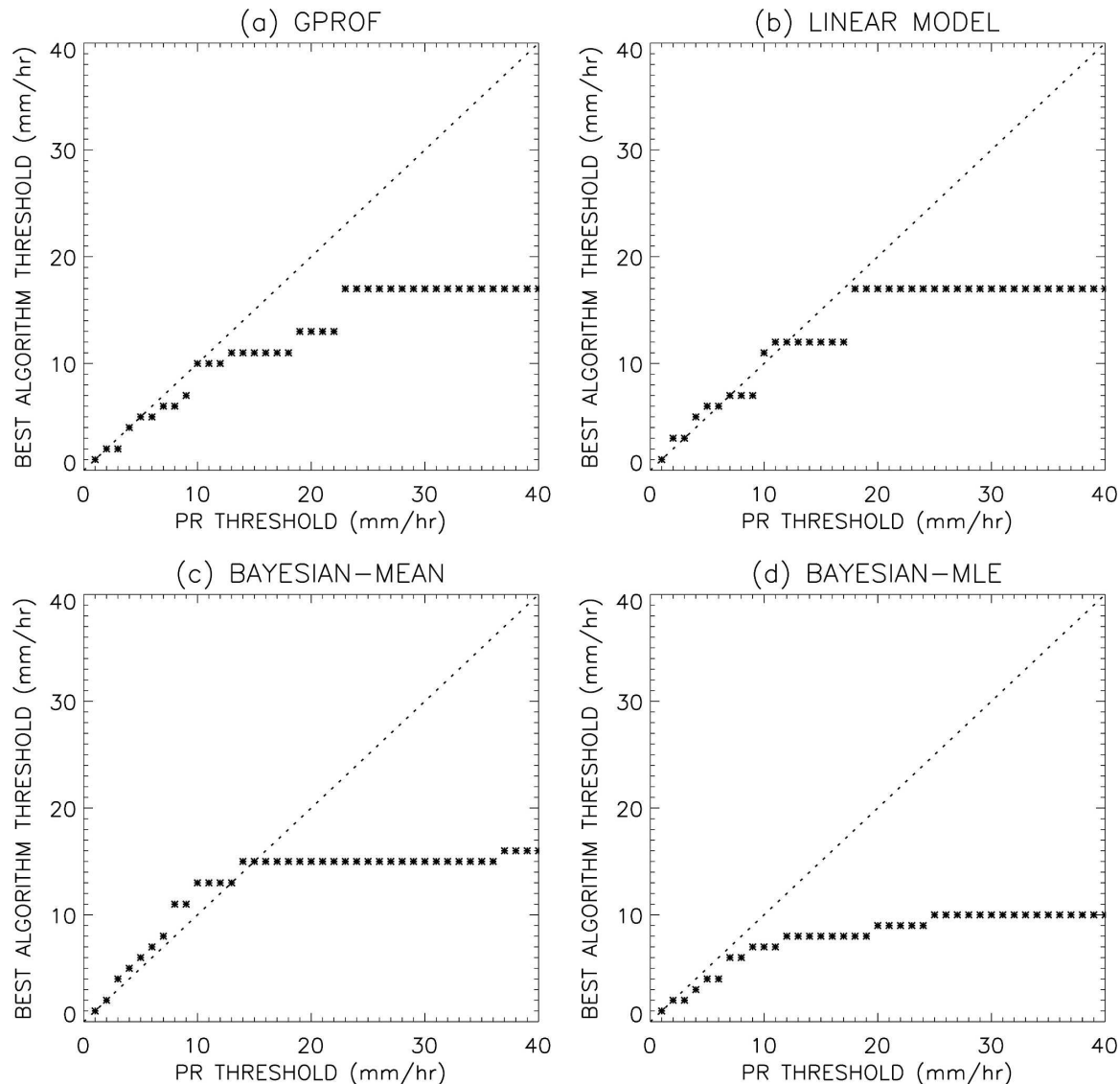


FIG. 12. Plots of the best algorithm rain-rate threshold with respect to the threshold of PR rain rate for the Bauer's cases with (a) GPROF, (b) the linear model, (c) Bayesian-MEAN, and (d) Bayesian-MLE.

ity distributions of rain rate from satellite microwave observations. The generic forms of this algorithm were composed of explicit, closed-form functions, and were based on simulations using high-resolution radar composites and a 1D plane-parallel radiative transfer model. From the derived posterior distributions, various statistical estimators, such as the mean and maximum likelihood estimate, can be used to serve as the single-pixel-retrieved rain rate, depending on the desired characteristics of the retrieval purpose.

We used synthetic randomly generated datasets to clarify the theoretical advantage of the Bayesian algorithm, as well as to demonstrate its retrieval ability when imperfect information was applied to the algo-

rithm, which is often the case in reality. We should be aware of the inherent retrieval uncertainty associated with certain scenes, especially in connection with variable beam-filling effects. In addition, a significant low bias at a higher rain rate is found even when the prior and conditional likelihoods are perfectly modeled. This bias is attributed to the loss of physically direct information concerning rain rate caused by the saturation of microwave observables. In such cases, the prior PDF supplies most of the information to the posterior PDF and favors the more frequent lesser rain rates.

The sensitivity tests revealed that retrieved surface rain rate is sensitive to assumptions in the prior rain-rate distribution. The effect of the prior distribution on

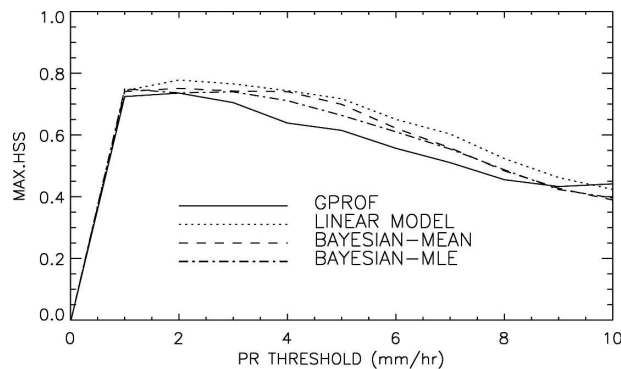


FIG. 13. Plots of the maximum Heidke skill score vs the PR rain-rate threshold in the range of  $[0, 10]$   $\text{mm h}^{-1}$  for Bauer's cases.

retrieval is different at various rain-rate ranges, mainly determined by the characteristics of the prior PDF. We also found that a simple covariance matrix is not sufficient to describe the statistical and physical dependency of microwave measurements on rain rate. This insufficiency can lead to substantial errors and bias in retrieval. On the other hand, a use of explicit functional models can provide more accurate and complete relationships without increasing computational loading. Once these explicit, closed-form functions are well fitted to the training dataset, the Bayesian algorithm is not very sensitive to the slight change in the parameterizations.

Applications to TMI data demonstrate that the performance of our Bayesian algorithm is comparable to that of GPROF and a new linear model, while ours also provides complete posterior rain-rate probability distributions. In general, retrievals from the Bayesian-MEAN algorithm have very small biases and good linear correlations with PR-derived rain rates. The Bayesian-MLE algorithm revealed an excellent ability to retrieve light rain intensity (shown in sensitivity tests as well). However, the maximum likelihood rain rate is generally much less than the expectation value obtained from the same posterior PDF, especially for higher rain rates. If unbiased averages over time and/or space are required, then the Bayesian-MEAN algorithm is the preferred choice. But, if more representative rain rates in areas of light rain are required in instantaneous “snapshots” of precipitating systems, the Bayesian-MLE result might be preferred.

We also found that our Bayesian algorithms had greater difficulty retrieving the heaviest rain rates. Large errors in retrieving heavy rain rates, even though the latter are relatively infrequent, can have large effects on computed root-mean-square errors and correlation coefficients. The inability of all algorithms to

achieve unbiased results in heavy rainfall is partly because of the fact that such events are not well represented in the respective databases. However, there is also an inherent limitation in the physical information content of microwave observations of heavy rainfall; saturation of the microwave signature forces even a “perfect” Bayesian algorithm to rely more heavily on the prior distribution in such cases, usually leading to underestimated retrievals.

As mentioned, because we limited our attention to a low-dimension problem, we were able to use explicit functions to provide complete posterior PDFs of rain rates from three microwave observables, and to better understand the strength of Bayesian approaches. We can consider applying our approach to a higher-dimension problem—that of retrieving entire hydrometeor profiles. A representative ensemble of datasets will be crucial to this issue.

**Acknowledgments.** This research was supported by NASA Grants NAG5-9894 and NNG04-GM77G.

#### REFERENCES

- Adler, R. F., C. Kidd, G. Petty, M. Morrissey, and H. M. Goodman, 2001: Intercomparison of global precipitation products: The Third Precipitation Intercomparison Project (PIP-3). *Bull. Amer. Meteor. Soc.*, **82**, 1377–1396.
- Alishouse, J. C., S. Snyder, and R. R. Ferraro, 1990: Determination of oceanic total precipitable water from the SSM/I. *IEEE Trans. Geosci. Remote Sens.*, **26**, 811–816.
- Bauer, P., and R. Bennartz, 1998: Tropical Rainfall Measuring Mission microwave imaging capabilities for the observation of rain clouds. *Radio Sci.*, **33**, 335–349.
- , P. Amayenc, C. D. Kummerow, and E. A. Smith, 2001: Over-ocean rainfall retrieval from multisensor data of the Tropical Rainfall Measuring Mission. Part II: Algorithm implementation. *J. Atmos. Oceanic Technol.*, **18**, 1838–1855.
- Chiu, J. C., 2003: Bayesian retrieval of complete posterior PDFs of rain rate from satellite passive microwave observations. Ph.D. thesis, Purdue University, 174 pp.
- Cho, H.-K., K. P. Bowman, and G. R. North, 2004: A comparison of gamma and lognormal distributions for characterizing satellite rain rates from the Tropical Rainfall Measuring Mission. *J. Appl. Meteor.*, **43**, 1586–1597.
- Conner, M. D., and G. W. Petty, 1998: Validation and intercomparison of SSM/I rain-rate retrieval methods over the continental United States. *J. Appl. Meteor.*, **37**, 679–700.
- Di Michele, S., A. Tassa, A. Mugnai, F. S. Marzano, P. Bauer, and J. P. V. P. Baptista, 2005: Bayesian algorithm for microwave-based precipitation retrieval: Description and application to TMI measurements over ocean. *IEEE Trans. Geosci. Remote Sens.*, **43**, 778–791.
- Evans, K. F., J. Turk, T. Wong, and G. L. Stephens, 1995: Bayesian approach to microwave precipitation profile retrieval. *J. Appl. Meteor.*, **34**, 260–279.
- Houze, R. A., and C.-P. Cheng, 1977: Radar characteristics of tropical convection observed during GATE: Mean properties

- and trends over the summer season. *Mon. Wea. Rev.*, **105**, 964–980.
- Ison, N. T., A. M. Feyerherm, and L. D. Bark, 1971: Wet period precipitation and the gamma distribution. *J. Appl. Meteor.*, **10**, 658–665.
- Jameson, A. R., and A. B. Kostinski, 1999: Fluctuation properties of precipitation. Part V: Distribution of rain rates—Theory and observations in clustered rain. *J. Atmos. Sci.*, **56**, 3920–3932.
- Kedem, B., and L. S. Chiu, 1987: Are rain rate processes self-similar? *Water Resour. Res.*, **23**, 1816–1818.
- , —, and G. R. North, 1990: Estimation of mean rain rate: Application to satellite observations. *J. Geophys. Res.*, **95**, 1965–1972.
- , R. Pfeiffer, and D. A. Short, 1997: Variability of space–time mean rain rate. *J. Appl. Meteor.*, **36**, 443–451.
- Kummerow, C., W. S. Olson, and L. Giglio, 1996: A simplified scheme for obtaining precipitation and vertical hydrometeor profiles from passive microwave sensors. *IEEE Trans. Geosci. Remote Sens.*, **34**, 1213–1232.
- , W. Barnes, T. Koza, J. Shiue, and J. Simpson, 1998: The Tropical Rainfall Measuring Mission (TRMM) sensor package. *J. Atmos. Oceanic Technol.*, **15**, 809–817.
- , and Coauthors, 2001: The evolution of the Goddard profiling algorithm (GPROF) for rainfall estimation from passive microwave sensors. *J. Appl. Meteor.*, **40**, 1801–1820.
- Liebe, H. J., G. A. Hufford, and T. Manabe, 1991: A model for the complex permittivity of water at frequencies below 1 THz. *Int. J. Infrared Millimeter Waves*, **12**, 659–675.
- Marshall, J. S., and W. M. Palmer, 1948: The distribution of raindrops with size. *J. Meteor.*, **5**, 165–166.
- Marzano, F. S., A. Mugnai, G. Panegrossi, N. Pierdicca, E. A. Smith, and J. Turk, 1999: Bayesian estimation of precipitating cloud parameters from combined measurements of spaceborne microwave radiometer and radar. *IEEE Trans. Geosci. Remote Sens.*, **37**, 596–613.
- , E. Fionda, P. Ciotti, and A. Martellucci, 2002: Ground-based multifrequency microwave radiometry for rainfall remote sensing. *IEEE Trans. Geosci. Remote Sens.*, **40**, 742–759.
- Nzeukou, A., and H. Sauvageot, 2002: Distribution of rainfall parameters near the coasts of France and Senegal. *J. Appl. Meteor.*, **41**, 69–82.
- Olson, W. S., C. D. Kummerow, G. M. Heymsfield, and L. Giglio, 1996: A method for combined passive–active microwave retrievals of cloud and precipitation profiles. *J. Appl. Meteor.*, **35**, 1763–1789.
- , and Coauthors, 2006: Precipitation and latent heating distributions from satellite passive microwave radiometry. Part I: Improved method and uncertainties. *J. Appl. Meteor. Climatol.*, **45**, 702–720.
- Petty, G. W., 1994a: Physical retrievals of over-ocean rain rate from multichannel microwave imagery. Part I: Theoretical characteristics of normalized polarization and scattering indices. *Meteor. Atmos. Phys.*, **54**, 79–100.
- , 1994b: Physical retrievals of over-ocean rain rate from multichannel microwave imagery. Part II: Algorithm implementation. *Meteor. Atmos. Phys.*, **54**, 101–121.
- Sauvageot, H., 1994: The probability density function of rain rate and the estimation of rainfall by area integrals. *J. Appl. Meteor.*, **33**, 1255–1262.
- Swift, J. L. W., and H. T. Schreuder, 1981: Fitting daily precipitation amounts using the Sb distribution. *Mon. Wea. Rev.*, **109**, 2535–2540.
- Tassa, A., S. Di Michele, A. Mugnai, F. S. Marzano, and J. P. V. P. Baptista, 2003: Cloud-model based Bayesian technique for precipitation profile retrieval from the Tropical Rainfall Measuring Mission Microwave Imager. *Radio Sci.*, **38**, 8074, doi:10.1029/2002RS002674.
- Wilheit, T. T., 1986: Some comments on passive microwave measurement of rain. *Bull. Amer. Meteor. Soc.*, **67**, 1226–1232.
- Wilks, D. S., and K. L. Eggleston, 1992: Estimating monthly and seasonal precipitation distributions using the 30- and 90-day outlooks. *J. Climate*, **5**, 252–259.